PASSIVE MICROWAVE PRECIPITATION DETECTION BIASES: RELATIONSHIP TO CLOUD PROPERTIES

A Thesis

by

ROBERT EDWARD MARTER JR.

Submitted to the Office of Graduate and Professional Studies of
Texas A&M University
in partial fulfillment of the requirements for the degree of

MASTER OF SCIENCE

Chair of Committee,	Anita D. Rapp
Committee Members,	Andrew E. Dessler
	Huilin Gao
Head of Department,	Ping Yang

December 2017

Major Subject: Atmospheric Sciences

ABSTRACT

Accurate measurement of the Earth's hydrologic cycle requires a more precise understanding of precipitation accumulation and intensity on a global scale. While there is a long record of passive microwave satellite measurements, passive microwave rainfall retrievals often fail to detect light precipitation or have light rain intensity biases because they cannot differentiate between emission from cloud and rain water. Previous studies have shown that AMSR-E significantly underestimates rainfall occurrence and volume compared to CloudSat. This underestimation totals just below 0.6 mm/day quasi-globally (60S-60N), but there are larger regional variations related to the dominant cloud regime. This study aims to use Moderate Resolution Imaging Spectroradiometer (MODIS) and the 94-GHz CloudSat Cloud Profiling Radar (CPR), which has a high sensitivity to light rain, with the Advanced Microwave Scanning Radiometer for Earth Observing System (AMSR-E) observations, to help better characterize the properties of clouds that lead to passive microwave rainfall detection biases. CPR cloud and precipitation retrievals, AMSR-E Level-2B Goddard Profiling 2010 Algorithm (GPROF 2010) rainfall retrievals, and MODIS cloud properties were collocated and analyzed for 2007-2009. MODIS cloud microphysical and macrophysical properties, such as optical thickness, particle effective radius, and liquid water path were analyzed when precipitation is detected by CloudSat and missed by AMSR-E. Results are consistent with past studies and show large passive microwave precipitation detection biases compared to CloudSat in stratocumulus and shallow cumulus regimes. An examination of cases where AMSR-E failed to detect precipitation detected by CloudSat shows that warm rain detection biases occur more frequently within lower LWP, τ, and CTH bins, but biases at higher LWP, τ, and CTH contribute more to the total frequency of missed precipitation. Warm rain detection biases occur more fre-

quently and biases contribute to more of the total frequency of missed precipitation for $r_e > 16$ μm. Cloud property-dependent thresholds were calculated and compared against Advanced Microwave Scanning Radiometer (Earth Observing System) (AMSR-E) Goddard Profiling Algorithm (GPROF). All cloud property-dependent brightness temperature (TB) thresholds showed improvements in hit rate and volumetric hit rates. Cloud property-dependent TB thresholds were investigated to determine if thresholds can be improved by separately constraining data to environmental and cloud regimes. Descent and stratocumulus regimes, which generally consist of warm clouds, showed further improvements of warm rain detection. Results suggest that aprori knowledge of cloud property information and environmental information could significantly improve the detection of warm precipitation in GPROF retrievals.

DEDICATION

To my parents, sister, wife, and all of those who have helped me along the way.

ACKNOWLEDGMENTS

I would like to thank my advisor, Dr. Anita Rapp for giving me the opportunity to attend graduate school. Her kindness and understanding, along with the many informative discussions that we had, has helped me become a better researcher and scientist, and for that, I am forever grateful. I would also like to thank my committee members Dr. Andrew Dessler and Dr. Huilin Gao for being a part of my journey through graduate school in the classroom and for taking the time to provide helpful feedback. I want to thank Tony for the endless amount of productive discussions that we had, for his assistance in teaching me IDL, and his help creating a combined satellite dataset. I must thank Kyle for his help with my many programming issues and being a great gym partner. Also, I would like to thank all of the friends that I have made during my time at Texas A&M. Without all of you this journey would not have been as amazing. Lastly, I would like to thank my parents, sister, and wife for all of their love and support.

CONTRIBUTORS AND FUNDING SOURCES

Contributors

This work was supported by a thesis committee consisting of Dr. Anita Rapp [advisor] and Dr. Andrew Dessler of the Department of Atmospheric Sciences and Dr. Huilin Gao of the Department of Civil Engineering.

Funding Sources

This research is supported by NSF Grant AGS-1128024 and NASA Grant NNX10AM21G

NOMENCLATURE

AMSR-E	Advanced Microwave Scanning Radiometer (Earth Observing System)
AVHRR	Advanced Very High Resolution Radiometer
CALIPSO	Cloud-Aerosol Lidar and Infrared Pathfinder Satellite Observations
CCN	Cloud condensation nuclei
CPR	Cloud Profiling Radar
CRM	Cloud resolving models
CSI	Critical Success Index
CTH	Cloud top height
DPR	Dual-frequency Precipitation Radar
DSD	Drop size distribution
ECMWF	European Centre for Medium-Range Weather Forecasts
EOS	Earth Observing System
FAR	False Alarm Rate
FL	Freezing level
GCOM-W1	Global Change Observation Mission-Water
GPM	Global Precipitation Measurement

GPROF	Goddard Profiling Algorithm
GSFC	Goddard Space Flight Center
hPa	Hectopascal
HR	Hit Rate
HSS	Heidke Skill Score
IFOV	Instantaneous field of view
IR	Infrared
ITCZ	Intertropical Convergence Zone
IWV	Integrated water vapor
LTS	Lower tropospheric stability
LWC	Liquid water content
LWP	Liquid water path
MISR	Multi-angle Imaging SpectroRadiometer
MODIS	Moderate Resolution Imaging Spectroradiometer
NASA	National Aeronautic and Space Administration
NSIDC	National Snow and Ice Data Center
OCO-2	Orbiting Carbon Observatory 2
OR	Odds Ratio
PIA	Path integrated attenuation

PMW	Passive microwave
PR	Precipitation Radar
r_e	Effective Radius
R04	Release 4 version
RAMS	Regional Atmospheric Modeling System
RF	Rain fraction
RSS	Remote Sensing Systems
SE	Southeast
SST	Sea surface temperature
TB	Brightness temperature
TMI	TRMM Microwave Imager
TPW	Total precipitable water
TRMM	Tropical Rainfall Measuring Mission
VHR	Volumetric Hit Rate
VIS	Visible
VOCALS-REx	VAMOS Ocean-Cloud-Atmosphere-Land Study Regional Experiment

TABLE OF CONTENTS

Page

LIST OF FIGURES

FIGURE Page

LIST OF TABLES

TABLE Page

1. INTRODUCTION

Precipitation is an important component of the hydrological cycle and exhibits large spatial and temporal variations. Latent heat released by precipitation accounts for three-fourths of the heat energy that the atmosphere receives (Simpson et al. 1996). It is the largest source of atmospheric heating in the tropics and is significant in higher latitudes as well (Wilheit 1986). More than two-thirds of global precipitation falls in the tropics (Hong et al. 1999) and is the main source of energy for driving the global atmospheric circulation (Simpson et al. 1988). Although light precipitation (< 1 mm hr^{-1}) accounts for 10% of the total amount of precipitation in the tropics, it accounts for 50% of total rain occurrence in the tropics and an even higher fraction in the mid-to-high latitudes (Kidd and Joe 2007).

Warm rain is underestimated and sometimes undetected using infrared (IR) techniques due to little variability between cloud top temperatures of raining and non-raining clouds (Nauss and Kokhanovsky 2006). Passive microwave (PMW) techniques may fail to detect warm rain due to a weak emission signal compared with deeper systems (Chen et al. 2011). A definitive estimation of global warm precipitation is difficult because previous studies (e.g., Petty 1999; Stephens et al. 2002; Rapp et al. 2009) may have different definitions of warm rain. Uncertainties in the estimation of global precipitation, due to observational and measurement challenges, also result in disagreements between different weather and climate models (Simpson et al. 1996). Stephens et al. (2010) found that major biases in model precipitation are a result of coarse resolution and uncertainties in the parameterization of warm rain processes. Suzuki et al. (2011) compared CloudSat and Moderate Resolution Imaging Spectroradiometer (MODIS) observed warm rain processes with two cloud resolving models (CRM). The observations indicated an initial growth stage where cloud water was present without drizzle or precipitation, but both models quickly con-

verted cloud water into larger sized particles, consistent with the shorter timescales for warm rain formation found by Suzuki and Stephens (2009). In addition, different cloud microphysics parameterization for warm rain processes, mostly autoconversion and accretion processes, lead to differences amongst the models. To have a more complete understanding of Earth's hydrological cycle and improve representation of precipitation processes, an accurate and continuous measurement of warm rain is necessary.

Low warm clouds generally cause Earth's climate system to cool due to their high albedo (Randall et al. 1984; Ma et al. 1996) and have significant effects on the radiation budget. Light precipitation from these clouds is primarily from warm rain. Warm rain is a result of the droplet coalescence process, occurs in liquid water clouds below the freezing level (FL), and is often observed in stratocumuli or well-developed trade wind and mid-latitude cumuli typically in the form of shallow ($>$3 km), isolated convective showers (Liu and Zipser 2009). These clouds have an abundant amount of liquid water, a sufficient updraft, and a prolonged lifetime to sustain collision-coalescence growth (Schumacher and Houze 2003). An air mass with tropical, maritime characteristics is ideal for these warm rain process to occur. Microphysical growth processes of cloud particles also play a role in rain rates from warm clouds (Suzuki et al. 2011). Extreme rainfall rates from the warm rain process can arise from the help of terrain or atmospheric boundaries as a source of low level atmospheric lift. The warm rain process is also influenced by the amount of cloud liquid water, while entrainment and mixing act to reduce it (Blyth et al. 2013).

Generally, rain in the tropics and precipitation in mid-latitude continental convection during cloud development originates as warm rain (Beard and Ochs III 1993). Liu and Zipser (2009) found that rainfall from warm precipitation features occurs mainly over the ocean, and was predominately observed in regions of large-scale subsidence, along windward coasts during the winter, and during the nighttime. It also dominates the total amount of tropical rainfall outside the Intertropical Convergence Zone (ITCZ), while mid-latitude

rainfall is predominately from ice clouds (Lau and Wu 2003, 2011; Lebsock and L'Ecuyer 2011). Liu and Zipser (2009) found that 20% of tropical rainfall is warm rain, however, drizzle and light rain were not included. King et al. (2015) found that rain falls globally from $\sim$ 25% of warm clouds detected by CloudSat and $\sim$ 27% of warm clouds simulated using the Regional Atmospheric Modeling System (RAMS).

Precipitation over land is estimated with the use of rain gauges and ground-based radar. Over the ocean, where ground-based radar measurements are sparse, precipitation estimates come almost completely from satellites. Currently, precipitation over the ocean is estimated with IR sensors, PMW sounders and imagers, and more recently, active microwave radars (cloud and precipitation radars). IR and visible (VIS) sensors are indirect indicators of precipitation, with colder temperatures, brighter targets, and higher cloud tops linked with presence of precipitation. Warmer temperatures (dimmer targets) are an indicator of lower cloud tops, and the lowest cloud tops are generally not associated with the presence of precipitation. These relationships between solar radiance or TB and precipitation may not be valid for different regions and seasons, have difficulties defining rain / no rain boundaries, cannot distinguish precipitation patterns at the mesoscale or smaller, and have significant limitations in detecting warm rain (Behrangi et al. 2010). Also, VIS techniques are only available during the daylight hours. Other satellite retrievals, especially scattering-based PMW, also have limitations that make it difficult to distinguish warm-topped clouds (Petty 1999).

PMW rainfall sensors use frequencies that range from 1 to 200 GHz. Microwave radiation can penetrate through non-precipitating clouds, although minor attenuation does occur (Westwater 1972). Hydrometeors in the atmosphere provide a direct relationship between PMW radiances observed from satellites and surface rainfall (Wilheit 1986). PMW sensors estimate rainfall rates in two regimes, an absorption regime and a scattering regime. The absorption regime estimates rainfall based upon emission from the Earth's surface

that is altered by the intervening atmosphere (Wilheit et al. 1977). This emission is dependent upon surface emissivity through Kirchoff's Law of thermal radiation. At microwave frequencies, oceans have a low uniform emissivity (~ 0.5) (Kummerow et al. 1996). The ocean provides a radiometrically cold background to help observe the "warm" radiation (higher TBs) emitted from hydrometeors. Over land, a much higher (~ 0.9) and more variable emissivity limits the use of PMW sensors to clouds with ice and requires a scattering regime to estimate rainfall rates. The ice scatters terrestrial radiation back towards the surface and creates cold areas in the imagery; however, this produces a less direct relationship to rainfall rate than in the absorption regime (Wilheit 1986).

The use of PMW retrievals to estimate rainfall does not come without limitations. PMW instruments are typically flown aboard low-altitude, polar-orbiting satellites. Polar-orbiting satellites provide a discontinuous temporal coverage at low altitudes and precipitation biases can occur in regions that experience a diurnal cycle of rainfall (Morrissey and Janowiak 1996). In addition, to offset the challenge of a weak energy source, a large instantaneous field of view (IFOV) is needed and results in a spatial resolution that is lower than some IR sensors (Chen et al. 2011). Small-scale showers and light precipitation can be difficult to detect due to a large footprint that infrequently takes measurements two to four times daily (Burdanowitz et al. 2015). Rapp et al. (2009) found that warm rain clouds may not entirely fill the large footprints and have too weak of an emission signal for warm rain to be detected. Biases in PMW rainfall retrievals can also arise due to assumptions made by retrieval algorithms. PMW retrievals have difficulties distinguishing between the emissions signals from cloud and rainwater at precipitation onset. Most retrieval algorithms address this issue by using a liquid water path (LWP) threshold, which Berg et al. (2006) and O'Dell et al. (2008) found can bias the data.

Spaceborne precipitation radars have a better spatial resolution than PMW sensors and are the most direct observation of precipitation. Precipitation radars are active microwave

sensors that send a microwave pulse towards a target, particularly hydrometeors and the Earth's surface, and measure the backscattered reflectivity as a function of distance. Rain rates are determined from profiling algorithms by utilizing the relationship between the backscattered signal and the cloud, precipitation, and surface properties (Mitrescu et al. 2010). However, errors occur due to attenuation of the signal and in finding a correct reflectivity-rainfall relationship (Simpson et al. 1996). The advantages of spaceborne radars include radar reflectivity being directly related to rainfall rate, observation of the three-dimensional structure of precipitation, and a single rain rate algorithm that works over ocean and land (Seto et al. 2005). In contrast to ground-based radars, spaceborne precipitation radars are unobstructed by terrain. Also, a higher frequency (lower wavelength) is used for spaceborne radars due to the smaller antenna required for space based platforms. All spaceborne radars have issues with surface clutter due to the signal reflecting off Earth's surface, and results below $\sim$ 750 m to 1 km must often be screened.

There have been three spaceborne cloud and precipitation radars, the Tropical Rainfall Measuring Mission (TRMM) Precipitation Radar (PR), Global Precipitation Measurement (GPM) Dual-frequency Precipitation Radar (DPR), and CloudSat Cloud Profiling Radar (CPR). While the TRMM PR has greatly improved our understanding of the tropical hydrological cycle, there are still issues in the detection of warm rain. The 13.8 GHz PR has a minimum detectable signal of $\sim$ 17 dBZ and minimum detectable rain rate of 0.7 mm hr^{-1} (Simpson et al. 1996), which is significantly higher than CloudSat's CPR low detectable rain rate. Low liquid water contents (LWCs), small drizzle droplets, and partial beam filling contribute to low reflectivities that may cause warm rain to go undetected by the PR (Lebsock et al. 2011). Also, in rain rate algorithms that utilize drop size distributions, the assumed drop size distribution is derived from the large end of the distribution causing signals from light precipitation to have significant inaccuracies. Kidd and Joe (2007) found that 50% of the total rainfall occurence from PR is less than 1 mm hr^{-1}.

Short and Nakamura (2000) estimate that as much as 20% of shallow rain is missed by the PR in the tropics. Behrangi et al. (2012) estimates that the PR detects only 40 to 60% of the tropical rain events detected by CloudSat, and in the subtropics, where warm rain is more dominant (Petty 1995), it is significantly lower.

The 94 GHz CloudSat CPR, launched in 2006, has a high sensitivity to cloud to help aid in the detection of cloud vs. rain. The CPR improves the detection of light precipitation with a minimum detectable signal of $\sim$ -30 dBZ. Fox and Illingworth (1997) found that 80 to 90% of marine stratocumulus clouds with LWP between 1 and 20 g m^{-2} are detected when a radar reflectivity threshold of -30 dBZ is used. Stephens et al. (2002) estimated that the CPRs 94 GHz frequency should be able to detect 80% of all water clouds. Validation of CPR rain estimates by Ellis et al. (2009) and Rapp et al. (2013) showed measurements that are similar with ship observations well into the high latitudes. Previous studies have also shown that the CPR improves upon the PR in areas where light precipitation occurs. Berg et al. (2010) examined rain frequency for both the CPR and PR in the TRMM region and found that CPR detects a rainfall frequency $\sim$ 2.5 times larger than PR. Behrangi et al. (2012) found that the PR misses a large fraction of rainfall in the subtropics, and particularly in stratocumulus regions, when compared to CloudSat's CPR. This study will use the enhanced sensitivity of the CPR to better understand warm rain biases in PMW retrievals from the AMSR-E.

PMW rainfall estimates over oceans are widely used because of the direct influence that hydrometeors have on microwave radiances, their large spatial coverage, and the long time series of observations. However, they have difficulties in detecting and measuring light precipitation due to its weak emission signal, its occurrence in small, shallow clouds that do not fill the IFOV, and difficulty in distinguishing the cloud from precipitation. Fig. 1.1 from Behrangi et al. (2012) shows a considerable underestimation of rainfall occurrence and volume by AMSR-E compared to CloudSat in the extratropics where light

precipitation is frequent.

This study focuses on trying to improve the detection and estimation of warm rain by

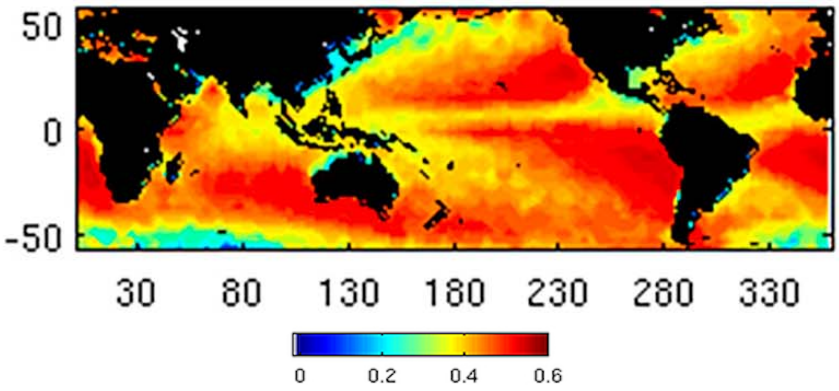

Figure 1.1: Map of fraction of rainfall missed by AMSR-E compared to CloudSat based on 3 years (2007-2009) of rainfall data (adapted from Behrangi et al., 2012).

PMW sensors by using additional information about the properties of clouds. Precipitation occurs when clouds have sufficient amount of water and cloud droplets become large enough to make it to the ground before evaporating (Guo et al. 2008; Duong et al. 2011). Because of this relationship, cloud properties have been related to the onset of precipitation. Chen et al. (2011) showed that optical thickness (τ) is highly correlated with CPR warm rain, but it can be come saturated in deep convective systems. An optically thick cloud with larger values of LWP will have a greater number of cloud droplets and liquid water available to help sustain the coalescence process. Previous studies (e.g., Stephens and Haynes 2007; Lebsock et al. 2008; L'Ecuyer et al. 2009) have suggested that larger LWPs are more likely to produce rain in warm clouds, which is likely why most PMW rainfall retrievals use LWP thresholds for the cloud to rain transition. Leon et al. (2008) shows that in stratocumulus regions, LWP values of 200 g m^{-2} were found to be drizzling

80 to 95% of the time. Similarly, Kubar et al. (2009) found that greater than 90% of warm clouds contain drizzle when LWP is > 250 g/m^2 and effective droplet concentration is low. In the far southeast (SE) Pacific, where warm clouds scarcely drizzle, greater than 90% contain drizzle if LWP > 200 g/m^2. The microwave ocean retrieval algorithm by Wentz (1997) uses a LWP precipitation threshold of 180 g m^{-1}, while other algorithms have used as high as 300 and 500 g m^{-1} (Curry et al. 1990). Wang et al. (2016) results show LWP precipitation thresholds regionally can vary from 150 to greater than 300 g/m^2, with the global mean LWP precipitation threshold ~ 190 g/m^2. Kubar et al. (2009) shows that drizzle frequency drastically increases with cloud top height (CTH) in all observed regions for warm clouds with heights less than 2 km. Also, drizzle frequencies greater than 80% are found in warm clouds with heights greater than 2 km in most regions. Warm clouds are shown to be drizzling 90 to 100% of the time when CTH > 3 km in regions where warm clouds can reach these heights. Snodgrass et al. (2009) stratified Multi-angle Imaging SpectroRadiometer (MISR) pixels by CTH and found that the amount of detectable rainfall rates in pixels with CTHs between 5.25 and 5.75 km is nearly twice the amount found in pixels with CTHs between 2.25 and 2.75 km. They also found that rainfall rates significantly increased with higher CTHs.

In addition to LWP and CTH thresholds, the presence of large droplets has also been used to detect precipitation, since it is more likely that precipitation will develop through coalescence. Many studies (e.g., Albrecht 1989; Rosenfeld and Gutman 1994; Lensky and Rosenfeld 1997) have proposed using an effective radius (r_e) of 14-15 μm as a precipitation onset threshold. Other studies (e.g., Gerber 1996; Masunaga et al. 2002; Shao and Liu 2004) have used 15 μm.

A study to determine the feasibility of using cloud properties as a predictor of warm precipitation was performed by Chen et al. (2011). Using CPR and AMSR-E rain rates it was estimated that AMSR-E underestimated warm rain in all clouds by 36.2%, predomi-

nately in clouds with top heights less than 3.5 km. Also, due to warm clouds below high clouds not being included in their study, this underestimation could be higher. Chen et al. (2011) analyzed MODIS cloud properties and CPR rain rates to determine rain / no rain thresholds and quantify their skill as a predictor of warm rain. LWP, τ, and r_e were tested and LWP was found to display the highest potential as a predictor. Chen et al. (2011) failed to analyze CTH, nor did they utilize AMSR-E rain estimates when determining skill scores for each cloud property. This study will expand upon Chen et al. (2011) and analyze missed warm rain and determine whether microphysical cloud property information can improve the current detection of warm rain by PMW sensors.

While there is a long record of passive microwave satellite measurements, PMW rainfall retrievals often fail to detect light, warm precipitation or have light, warm rain intensity biases because they cannot differentiate between emission from cloud and rain water. Previous studies (Behrangi et al. 2012) have shown that AMSR-E significantly underestimates rainfall occurrence and volume compared to CloudSat. This underestimation totals just below 0.6 mm/day quasi-globally (60S-60N), but there are larger regional variations related to the dominant cloud regime. This study aims to use the collocated measurements of AMSR-E with the CloudSat CPR and MODIS to first characterize the properties of clouds that lead to passive microwave rainfall detection biases and ultimately determine their potential for use as input or constraints to improve the detection of light, warm rain.

The main goals of this study are to:

1. Analyze properties of clouds and quantify precipitation detection biases between AMSR-E and CloudSat.

2. Create cloud property dependent TB thresholds and compare with current rainfall retrieval thresholds (e.g., Kummerow et al. 2011; Miller and Yuter 2013; Wentz 1997)

3. Determine whether and where cloud property information could be used to improve the AMSR-Es detection of warm precipitation.

4. Quantify the volume of warm precipitation detected using additional cloud property information.

2. DATA AND METHODS

This study uses a combination of active and passive instruments onboard satellites, shown in Table **??**, that are a part of the Earth Observing System (EOS) afternoon constellation, commonly referred to as the A-Train. It consists of six satellites including Orbiting Carbon Observatory 2 (OCO-2), Global Change Observation Mission-Water (GCOM-W1), EOS Aqua, Cloud-Aerosol Lidar and Infrared Pathfinder Satellite Observations (CALIPSO), CloudSat, and EOS Aura seen in Fig. 2.1. A-Train satellites are flown at an altitude of $\sim$ 705 km with an inclination of $\sim$ 98.14 degrees and are spaced seconds to minutes apart from one another. They fly in a sun-synchronous orbit where they cross over the equator at a mean local time range of 1:30 pm and 2:00 pm. A-Train satellites can view the Earth in an extensive range of wavelengths, and together with the simultaneous measurement of different climate parameters and different scanning patterns of instruments, provide valuable information about the Earth's changing climate (L'Ecuyer and Jiang 2010). A-Train satellite observations are collocated and matched from 2007-2009 to better understand the relationship between cloud properties and PMW warm rain detection biases.

2.1 CloudSat CPR

The CloudSat CPR, launched in 2006, is a 94-GHz nadir-looking active radar that measures radiation backscattered by clouds as a function of distance from the radar. It trails CALIPSO by $\sim$ 103 seconds and Aqua by $\sim$ 3 minutes. The CPR has an along track by across track resolution of 1.7 km X 1.4 km, respectively, and a minimum detectable reflectivity of $\sim$ -30 dBz. The low detectable reflectivity helps aid in the detection of cloud vs rain, but heavy rain rates can lead to an underestimation of precipitation due to a complete saturation of the CPR surface return. Also, since the CPR is a nadir looking radar and

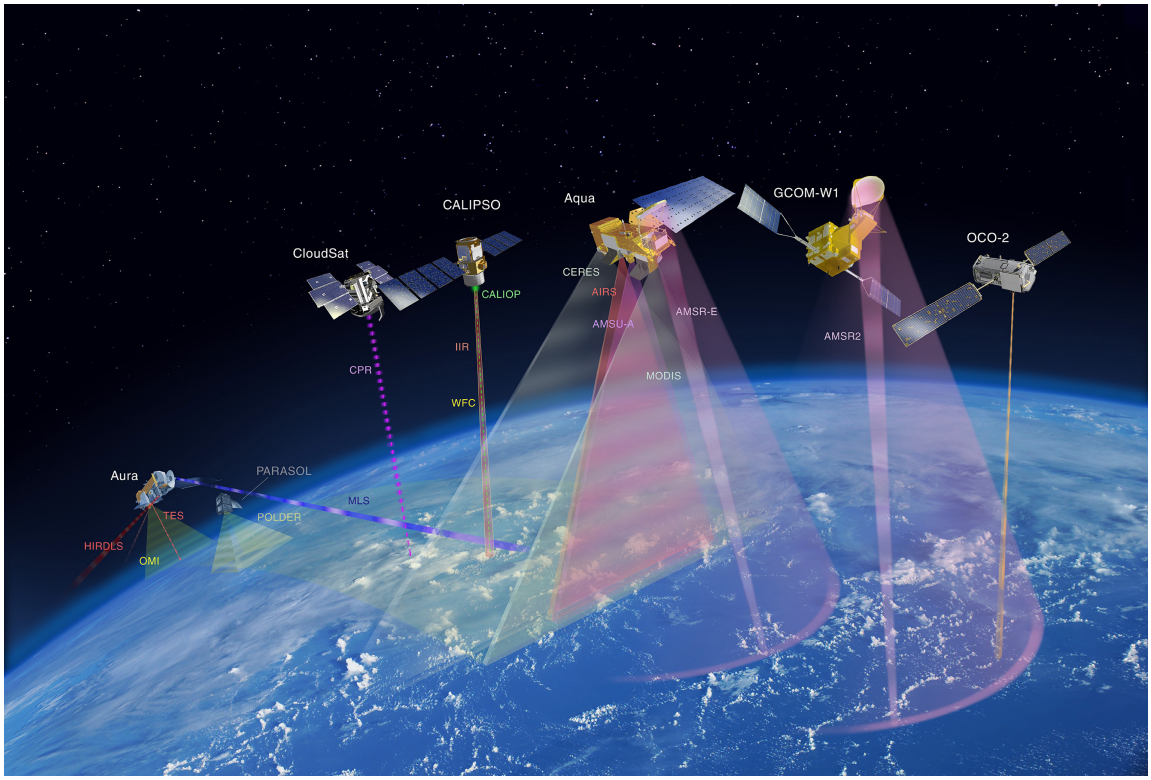

Figure 2.1: The A-Train constellation. Instrument footprints are shown with dashed lines indicating an active instrument and solid lines indicating a passive instrument. Instrument swaths are color-coded based off the wavelength range it observes. Swaths operating in microwave wavelengths are illustrated as red-purple to deep purple, solar wavelengths as yellow, solar and IR wavelengths as gray, and other IR wavelengths as red.
(reprinted from https://atrain.nasa.gov/)

not a scanning radar, it can only collect a single vertical profile along the flight direction. The CloudSat CPR data products used in this study include 1) the combined CloudSat and CALIPSO 2B-GEOPROF-LIDAR, 2) 2C-PRECIP-COLUMN (Haynes et al. 2009), and 3) 2C-RAIN-PROFILE (L'Ecuyer and Stephens 2002).

The 2B-GEOPROF-LIDAR product combines both CloudSat's and CALIPSOs abilities to better detect the occurrence and structure of Earth's hydrometeor layers (Mace and Zhang 2014). The release 4 version (R04) of the combined CloudSat radar and CALIPSO

(Winker et al. 2009) lidar 2B-GEOPROF-LIDAR (Mace and Zhang 2014) product is used to define CTH and the number of cloud layers. Algorithm outputs from the R04 2C-PRECIP-COLUMN product developed by Haynes et al. (2009) are listed in Table **??** and are used to limit clouds to below the FL (warm clouds) and only include pixels with a high certainty of warm rain (Precip_flag = 3).

CPR-retrieved rain rates are from 2C-RAIN-PROFILE (L'Ecuyer and Stephens 2002) R04 (Mitrescu et al. 2010) that was modified by (Lebsock and L'Ecuyer 2011), which uses rainfall drop size distributions (DSDs) and vertical distribution assumptions along with the path integrated attenuation (PIA) and observed reflectivity profile. These CPR rain rates are used to create a rain fraction (RF) data set that indicates the fraction of CPR pixels matched within an AMSR-E footprint that are precipitating. Ellis et al. (2009) validated CPR rain estimates by showing measurements that are similar with ship observations well into the high latitudes. Also, Rapp et al. (2013) found CPR rain estimates in the SE Pacific to be in good agreement with in situ radar estimates from the VAMOS Ocean-Cloud-Atmosphere-Land Study Regional Experiment (VOCALS-REx) in both frequency and distribution of precipitation. All data products are available at CloudSat data processing center (http://www.cloudsat.cira.colostate.edu).

2.2 AMSR-E

AMSR-E, operational from 2002-2011, is a conically scanning, dual-polarized PMW radiometer on the Aqua satellite. Earth-emitted microwave radiation is observed at frequencies ranging from 6.9 to 89 GHz with vertically and horizontally polarized measurements at each frequency. Spatial resolutions range from 5.4 km at 89 GHz to 56 km at 6.9 GHz. AMSR-E makes 486 observations per approximately 2000 scans at 89 GHz and 243 observations at all other frequencies. The AMSR-E data products in this study include

Data		
Sensors	Data Products	Variables
AMSR-E	AE_RAIN AE_L2A	Rain Rate TB
CloudSat CPR	2B-GEOPROF-LIDAR 2C-PRECIP-COLUMN 2C-RAIN-PROFILE	CloudLayers and LayerTop FL and Precip_Flag Rain Rate and Navigation_Land_Sea_Flag
MODIS	MOD06_L2	LWP, r_e, τ, and Cloud phase optical properties

Table 2.1: Data products

the National Snow and Ice Data Center (NSIDC) AMSR-E/Aqua L2B Global Swath Rain Rate/Type Goddard Space Flight Center (GSFC) Profiling Algorithm (AE_RAIN) Version 2 (Adler et al. 2004) and NSIDC AMSR-E/Aqua L2A Global Swath Spatially-Resampled Brightness Temperatures (AE_L2A) Version 2 (Ashcroft and Wentz 2006). AMSR-E TBs are from the AE_L2A algorithm that uses weighted coefficients to resample Level-1A antenna temperatures to a set of common spatial resolutions. A matched AMSR-E TB and CloudSat dataset was provided by Dr. Mark Kulie at Michigan Tech University. AMSR-E rain rates from the AE_RAIN retrieval algorithm were matched with this dataset over oceans.

2.2.1 GPROF

PMW rain rates in this study are from GPROF. The GPROF algorithm uses a Bayesian inversion methodology (Eq (2.1)) discussed in Kummerow and Ferraro (2007):

$$P_r(R|TB) = P_r(R) \times P_r(TB|R) \tag{2.1}$$

where $P_r(R)$ is the probability that a rain profile R will be observed and $P_r(TB|R)$ is the probability of observing the set of TBs given a rain profile R. The first term on the right hand side of equation (2.1) is acquired using CRMs and the second term on the right hand side of equation (2.1) is the TB that matches with the CRM output from radiative transfer schemes. CRM simulations and coupled radiative transfer calculations create an a priori database of hydrometeor profiles and associated TBs (Kummerow et al. 2001). However, there is a not a guarantee that CRMs correctly depict the observed profile. This work uses AE_RAIN rain rates from the GPROF 2010 algorithm (Kummerow et al. 2011), which takes advantage of an observationally based a priori database consisting of TRMM PR and TRMM Microwave Imager (TMI) observations, including surface wind, total precipitable water (TPW), LWP, and sea surface temperature (SST), along with CRM simulations and radiative transfer calculations. All TRMM pixels are compared to original database, and so rain screens and convection/stratiform separations are no longer necessary. In addition, the database is also constrained by SST and TPW when searching for potential solutions.

2.3 MODIS

MODIS flies onboard both the Terra and Aqua satellites and takes measurements of the atmosphere, land, and ocean. Aqua was launched into orbit by National Aeronautic and Space Administration (NASA) in 2002. Data is collected in 36 spectral bands that range from visible (0.4 μm) to thermal infrared (14.4 μm). MODIS has a continually rotating double sided scan mirror that scans 2330 km swaths at $\pm$ 55°. It has a high spatial resolution of 250 m (bands 1-2), 500 m (bands 3-7), and 1 km (bands 8-36). Retrieved cloud optical properties, including LWP, τ, and r_e, along with a cloud phase optical properties variable are from the MODIS MYD06_L2 Cloud Product (King et al. 1997), and were previously collocated to the CloudSat track. The cloud phase optical properties variable

was used to limit the data to liquid water clouds only. The MYD06_L2 product has a 1 km pixel resolution, and the cloud optical properties are only available during the daytime. The detection of cloud optical properties and cloud phase (determined from τ, r_e, and derived LWP retrievals) comes from an algorithm that utilizes reflected solar radiation measurements at multiple wavelengths through a combination of a lookup table approach, interpolation, and asymmetric theory (King et al. 1997).

2.4 Methodology

2.4.1 Matching Process

A-train satellite observations are collocated and matched from 2007-2009. Each instrument has a different pixel resolution and thus all pixels are matched along the CloudSat track. A MODIS data set previously collocated to the CloudSat track was combined with the AMSR-E AE_RAIN rain rates by matching all CloudSat CPR dataset pixels to the closest AMSR-E pixel utilizing geolocation and time parameters. The AMSR-E TB dataset matched to the CloudSat track was also combined with the existing matched dataset. Because of resolution differences, each AMSR-E footprint will have multiple CPR footprints matched to it. A RF dataset was created by calculating the percent of all matched CPR pixels that are precipitating within an AMSR-E pixel. For every AMSR-E pixel there are retrieved rain rates and TBs, along with matched CPR rain rates and MODIS cloud property information.

2.4.2 Data Screening

To study precipitation detection in warm clouds, analysis of data is only performed for water clouds over the ocean where CloudSat detects precipitation with a high certainty (Table **??**). Once the matching process is completed, data goes through a series of con-

straints by the process shown in Fig. 2.2. A Navigation_land_sea_flag value of 2 from 2C-RAIN-PROFILE was applied to restrict the data to only over the ocean. This criteria helps eliminate any contamination of highly variable TBs that occur over land. Next the dataset is screened to only include warm clouds. Criteria were applied where CTH must be less than the FL and only a single cloud layer is being observed (CloudLayers = 1). Also, a latitude range of 60° N and 60° S is analyzed since very few clouds outside of this range have no ice contamination.

AMSR-E misses precipitation when it does not detect precipitation that the CPR detects. Thus at least one of the CPR pixels must be precipitating to determine when AMSR-E misses, and the data is constrained to only pixels where CPR rain rate is greater than 0. To ensure that the CPR-estimated rain rates are the highest quality, a precipitation flag is applied to only analyze pixels that have a high certainty of rain. A RF of 100 dataset is created to only include data where all of the CloudSat pixels inside an AMSR-E footprint are precipitating. AMSR-E frequently misses or underestimates precipitation cells that do not fill the entire IFOV, and so this dataset will help mitigate some of the beamfilling error. The RF = 100 dataset is used to create missed precipitation histograms and cloud property dependent TB thresholds. Also, cloud property dependent thresholds are applied to the RF = 100 dataset for statistics calculations. If data is not screened by RF = 100, then the dataset is referred to as RF = ALL since data of all RFs are included. Cloud property dependent thresholds are applied to the entire RF = ALL dataset for statistical calculations. Also, thresholds are applied to data that is constrained by RF range using the RF = ALL dataset.

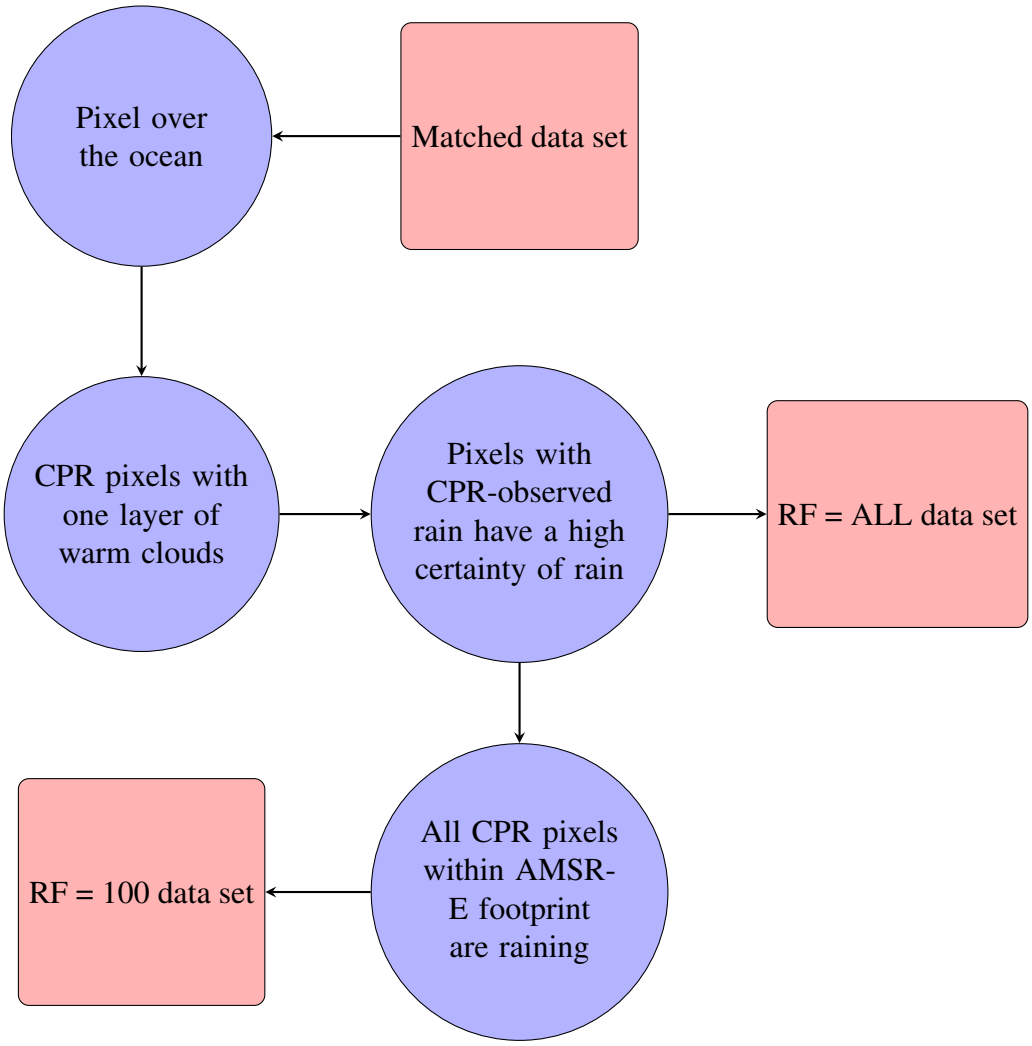

Figure 2.2: Flow chart of data screening process

Criteria	Summary
Navigation_Land_Sea_Flag = 2	Data points only occur over the ocean
60° N to 60° S	Data points are between 60° N to 60° S
CloudLayers = 1	A single cloud layer
CTH $<$ FL	Tops of clouds are lower than the FL
CPR rain rate $>$ 0	CloudSat CPR pixels are precipitating
Precip Flag = 3	High certainty of warm rain from CloudSat
RF = 100	All of the CloudSat CPR pixels inside an AMSR-E footprint are precipitating

Table 2.2: Data screening

2.4.3 Missed Warm Rain Biases

Analysis of cloud properties is performed for missed warm precipitation, which is defined as when all matched CloudSat pixels are precipitating, but AMSR-E is not (RF = 100). Histograms of missed precipitation frequencies were calculated to help assess which cloud properties might be best to improve the detection of precipitation onset. Total relative frequencies were calculated to show the occurrence of certain cloud property values when precipitation is missed. For example, total relative frequencies for LWP are calculated by the following equation:

$$\text{Total Relative Frequency} = \frac{\begin{array}{c}\text{\# of pixels when AMSR-E misses rain and} \\ \text{CPR detects rain for a specific LWP value}\end{array}}{\begin{array}{r}\text{Total \# of pixels when AMSR-E misses rain and} \\ \text{CloudSat detects rain}\end{array}} \tag{2.2}$$

and total relative frequencies are also calculated for all cloud properties. In addition to the total relative frequencies, value dependent relative frequencies were calculated to show how often warm precipitation is missed when a specific cloud property value is observed. Pixels are collected similar to the previously mentioned LWP frequencies, but value de-

pendent frequencies have a different calculation shown by the following equation:

$$\text{Value Dependent Frequency} = \frac{\begin{array}{c}\text{\# of pixels when AMSR-E misses rain and} \\ \text{CPR detects rain for a specific LWP value}\end{array}}{\begin{array}{c}\text{\# of pixels when CloudSat} \\ \text{detects rain for the same LWP value}\end{array}} \tag{2.3}$$

and value dependent frequencies are also calculated for all cloud properties. Lastly, the mean cloud properties when warm rain is missed for every latitude and longitude are calculated and mapped. These plots are analyzed to determine where these missed warm precipitation biases occur and the spatial variability in the different cloud properties for missed precipitation.

2.4.4 Cloud Property Dependent TB Threshold Creation

The goal of this study is to determine if the addition of cloud property information into GPROF can help improve warm rain detection. It is beyond the scope of this project to create a completely new GPROF database sorted by cloud properties to test whether they help GPROF retrievals. This study instead will create cloud property dependent TB thresholds by modifying a simplified drizzle detection method by Miller and Yuter (2013), that originally used TBs and integrated water vapor (IWV). Miller and Yuter (2013) found a correlation between horizontally polarized 89 GHz TBs (T89H) and IWV that shows, when plotted in both cloud-free and stratocumulus regions with overlaid LWP contours, a TB threshold can be calculated that reasonably separates drizzling from non-drizzling pixels. Their IWV dependent TB threshold can be seen as the dashed line in Fig. 2.3. Here we will test whether using TBs together with cloud properties could potentially lead to improvements if a PMW retrieval algorithm has the properties a priori as an input.

Cloud properties that exhibit missed warm precipitation biases are plotted as a function of TBs in 2-D histograms, like the example shown in Fig. 2.4. Each bin is calculated by dividing CPR detected precipitation by missed AMSR-E precipitation and gives a frac-

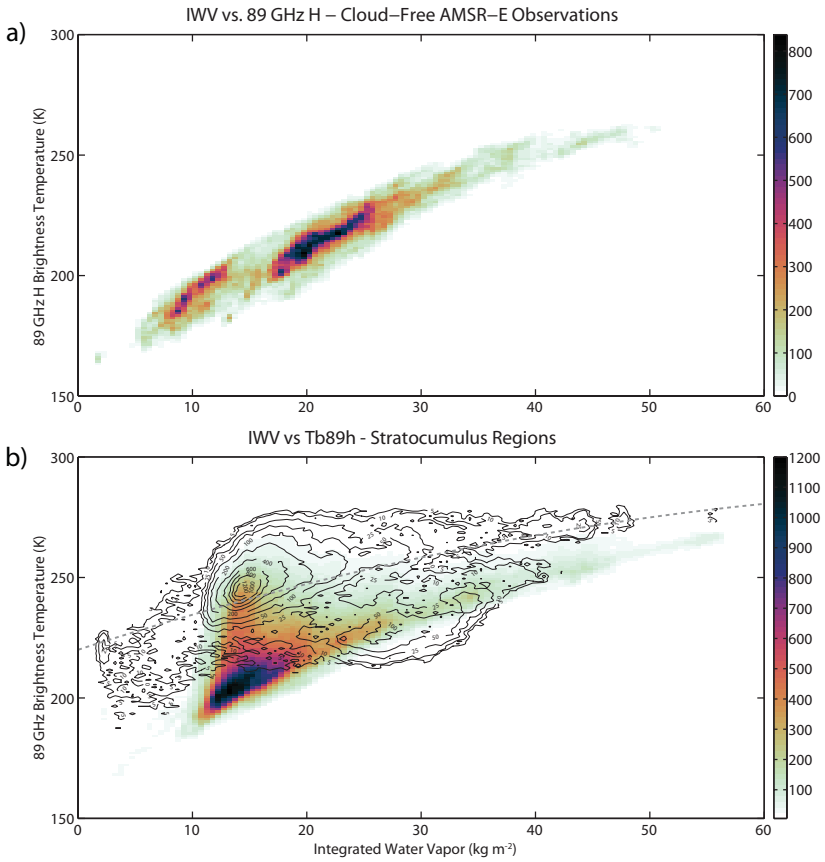

Figure 2.3: **(a)** Scatter density plot of IWV versus T89H for cloud-free AMSR-E pixels from randomly selected scenes between 60N and 60S latitude. **(b)** Scatter density plot of IWV versus T89H for 4,409,366 pixels from 45 randomly selected marine stratocumulus scenes containing detectable drizzle. The contours denote the counts for the subset of points with LWP values $\geq$ 200 g m^{-2}. The dashed grey line denotes the threshold curve for drizzle classification (reprinted from Miller and Yuter, 2013).

tion from 0 to 1 of missed precipitation. Thus, each bin displays the fraction of missed precipitation relative to precipitation detected by CloudSat for a given TB and cloud property variable. The next step in creating a threshold is using a target fraction of missed precipitation as points along the threshold line. For example, a target fraction of 0.5 was selected in Fig. 2.4 for each column. If one point with a fraction of 0.5 is found then it is selected as a threshold data point. If more than one point is found then an average

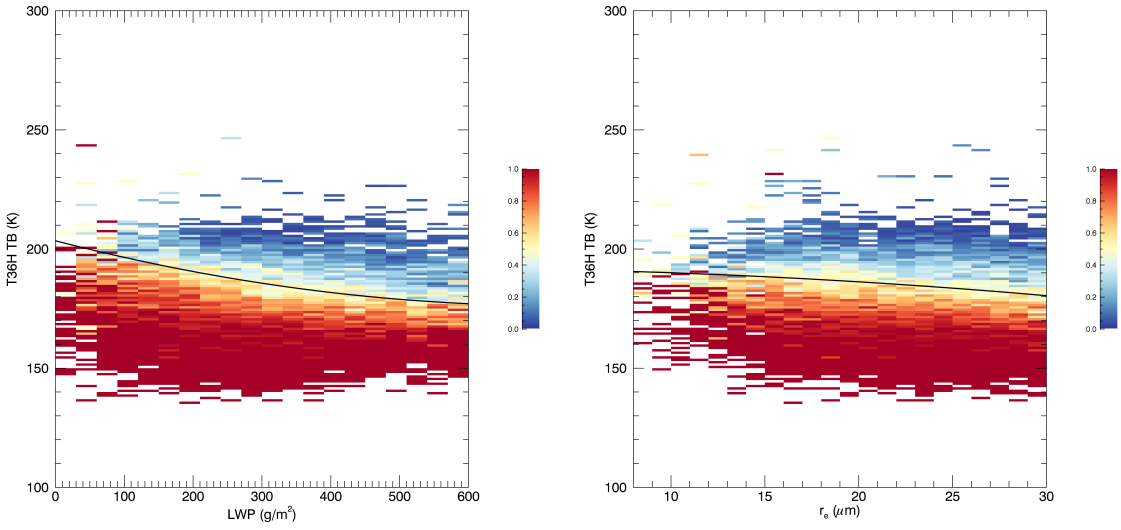

(a) (b)

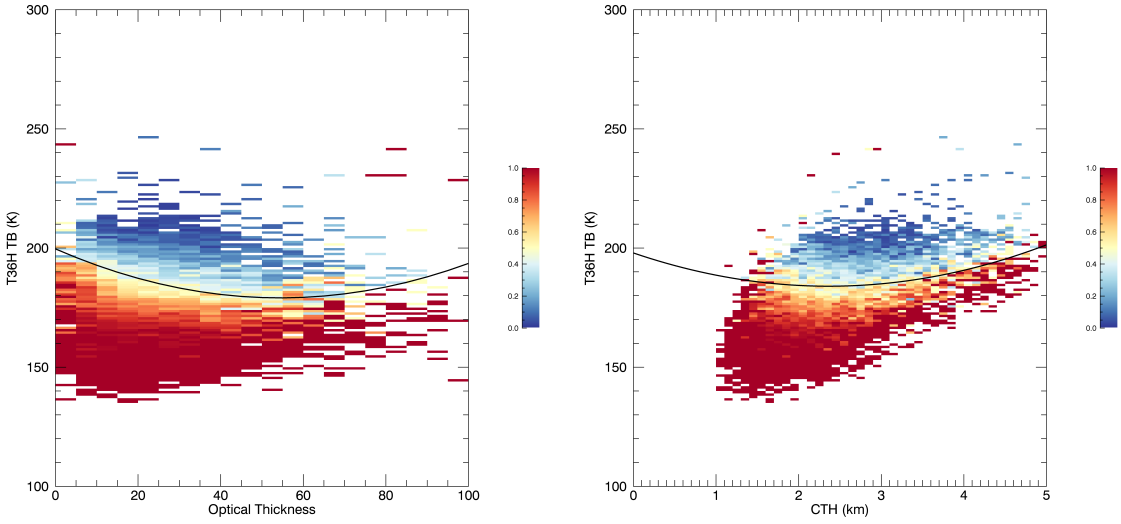

(c) (d)

Figure 2.4: 2-D histogram of 36H GHz TB vs. **(a)** LWP, **(b)** r_e, **(c)** τ, and **(d)** CTH with missed AMSR-E precipitation fraction plotted and a target fraction of 0.5 used. Solid black line indicates threshold created.

of points is taken. This process is repeated for each column, and then a linear regression is performed using a least-square polynomial fit on these data points. A cloud property dependent TB threshold is created and the resulting equation is:

$$TB_{threshold} = a(X)^2 + b(X) + c \tag{2.4}$$

where a, b, and c are coefficients and *X* is the cloud property value. Once the threshold is created, this procedure is repeated for other target fractions in increments of 0.05 up to 0.95. All of the thresholds are overlaid on the 2-D histograms plots as a solid black curve similar to Fig 2.4. Both polarizations of the 89 GHz and 36 GHz channels were analyzed. After thresholds are created for all combinations of cloud variables and target missed fractions, detection statistics are calculated and compared to existing techniques and the current AMSR-E algorithm.

2.4.5 Detection Statistics

The main goal of this study is to investigate whether cloud property information can be useful in aiding the detection of warm precipitation by PMW sensors. We aim to achieve this by creating thresholds of TB with varying cloud properties. If a pixel with a given cloud property value and TB is above the threshold, then the pixel is identified as precipitation. If the pixel is below the threshold it is not identified as precipitation. After thresholds are applied it is crucial to examine detection statistics to determine whether improvements can be made. To achieve this, a 2 $\times$ 2 contingency table is used. The 2 $\times$ 2 contingency table, shown in Table 2.3, can be used for forecasting whether an event will occur, and in this case, whether a threshold correctly predicts precipitation. The variables a, b, c, and d are counts. The forecast is the threshold, with data above the threshold indicating a forecast of precipitation and data below the threshold indicating a forecast of no

Table 2.3: 2 X 2 contingency table

	Event Observed	Event Not Observed	Total
Event Forecasted Yes	a	b	a + b
Event Forecasted No	c	d	c + d
Total	a + c	b + d	n= a + b + c + d

precipitation. The event that is observed or not observed is CPR rain. Variable a is when CPR-observed precipitation is correctly predicted by the threshold and is referred to as a hit. Variable b is when CPR does not detect precipitation, but the threshold incorrectly predicts precipitation, referred to as a false alarm. Variable c is when CPR-observed precipitation is not predicted by the threshold and referred to as a miss. Variable d is when the threshold correctly predicts no precipitation and is sometimes referred to as a correct negative. With the 2 $\times$ 2 contingency table and counts of hits, misses, and false alarms, statistics can be computed to better understand how good of a predictor the threshold is (Wilks 2011). First, skill scores are calculated to quantify the skill of prediction. The Heidke Skill Score (HSS),

$$HSS = \frac{2(ad - bc)}{(a + c)(c + d) + (a + b)(b + d)} \tag{2.5}$$

is a measure of skill of a forecast (threshold) compared with a standard forecast (chance). HSS ranges from -∞ to 1. A score of 1 equals a perfect forecast, and thus the created threshold perfectly predictions warm precipitation. A score of 0 indicates the skill of the created threshold is no better than chance, and a negative score indicates that a chance forecast would be a better predictor of warm precipitation. Critical Success Index (CSI),

$$CSI = \frac{a}{a + b + c} \tag{2.6}$$

is the number of times a threshold correctly predicts precipitation divided by the total number of occasions the threshold predicts precipitation and/or CPR observes precipitation. It was originally called the ratio of verification by Gilbert (1884) and sometimes referred to as the Gilbert Score. CSI can be seen as the proportion correct after removing cases in which the threshold correctly predicts no precipitation. A score of 0 is the worst that can be received and a score of 1 is the best.

Other statistics were also calculated to quantify the accuracy of the forecast and improvements of detection of precipitation occurrence and volume. The odds ratio (OR),

$$OR = \frac{ad}{bc} \tag{2.7}$$

is the product of correct forecasts divided by the product of incorrect forecasts. It is also the conditional odds of a hit given that the CPR predicts precipitation over the conditional odds of a false alarm given that the CPR does not detect precipitation. Larger values indicate a more accurate forecast. Bias,

$$Bias = \frac{a+b}{a+c} \tag{2.8}$$

is the ratio of number of times the threshold predicts precipitation to the number of times CPR observes precipitation. An unbiased predictor would have a value of 1, which indicates that the threshold predicts precipitation the same amount of times that CPR observed it. A value greater than 1 indicates that the threshold predicts precipitation more often than CPR observes precipitation and is called over-forecasting. A value less than 1 indicates that the threshold predicts precipitation less often than CPR observes precipitation and is

called under-forecasting. The hit rate (HR),

$$HR = \frac{a}{a+c} \tag{2.9}$$

is the ratio of forecasts in which the threshold correctly predicts precipitation to the number of times CPR observes precipitation. It is also referred to as the probability of detection. Larger values are preferred with 0 being the worst and 1 the best. The false alarm rate (FAR),

$$FAR = \frac{b}{b+d} \tag{2.10}$$

is the ratio of forecasts in which the threshold incorrectly predicts precipitation to the number of times CPR does not observe precipitation. It is also referred to as the probability of false detection.

A volumetric hit rate (VHR) is calculated using the same formula as equation (2.9), but instead of a count, the volume of precipitation is totaled for each variable. Volumetric statistics are limited to hit rate because for all other statistics to be computed, a volume is required for when CloudSat does not detect precipitation which will always be 0. HRs, FARs, and VHRs are expressed as percentages for this study.

3. RESULTS

Once data are matched and constrained it is plotted for comparison with Fig. 1.1. The fraction of missed warm precipitation is calculated by finding all of the pixels where all of the CPR rain rates in an AMSR-E footprint are greater than 0 and AMSR-E rain rate is equal to 0, then dividing it by the total number of AMSR-E pixels where CPR indicates it is raining. These calculations are performed in $5^\circ \times 5^\circ$ boxes and plotted globally. Fig. 3.1 shows a large fraction of missed warm precipitation in the areas where a large fraction of AMSR-E misses are shown in Fig. 1.1 suggesting that warm precipitation is a large contributor to the global amount of missed rain. These misses mostly occur in subsidence regimes off the western coasts of the continents where stratocumulus clouds and light, warm precipitation are prominent.

Mean CPR rain rates when AMSR-E misses precipitation are calculated for each $5^\circ \times 5^\circ$ bin and plotted in Fig. 3.2. Fig. 3.2 shows that when AMSR-E misses warm precipitation, low precipitation rates are measured in the same subsidence and stratocumulus regimes where AMSR-E has a high fraction of misses. This is consistent with what we would expect since AMSR-E has difficulties in distinguishing the difference between the emission signal for cloud and precipitation at precipitation onset.

3.1 Cloud Property Histograms

Figures 3.1 and 3.2 show that AMSR-E frequently misses warm precipitation in regions where stratocumulus clouds are prominent and rain rates are low, and thus, AMSR-E often fails to determine precipitation onset. Previous literature suggests that cloud properties, such as LWP and r_e, can be used as possible thresholds for precipitation onset. Cloud properties that are physically linked with precipitation and show large fractions of missed

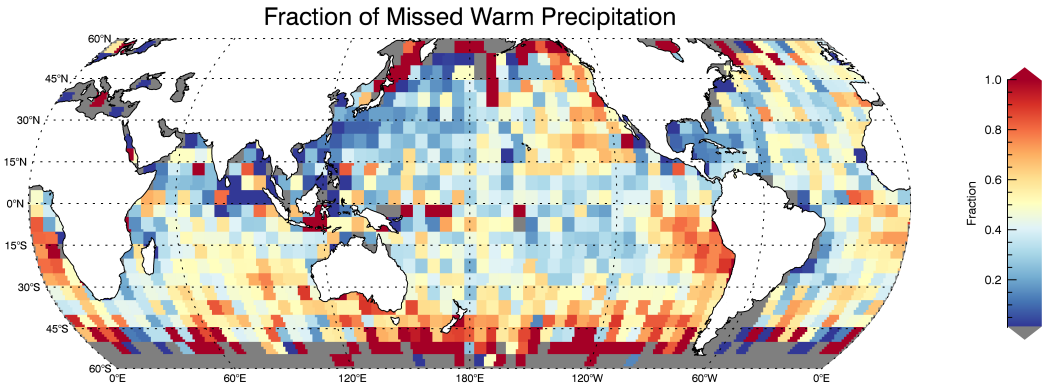

Figure 3.1: Map of fraction of warm precipitation missed by AMSR-E. It is based on 3 years (2007-2009) of rainfall data and RF = 100.

precipitation can help determine which, if any, would be best suitable to be used as a threshold for precipitation onset. An initial examination of missed warm precipitation was performed for selected cloud properties. In addition to LWP and r_e, CTH and τ were also used for this study. To accomplish this, two different histograms were calculated for each cloud property. A histogram of seasonal and total relative frequencies of MODIS cloud properties and CloudSat-CALIPSO CTHs when AMSR-E misses precipitation is shown in Fig. 3.3. The frequency of a given cloud property value is calculated when AMSR-E misses warm precipitation and then cloud property histogram bins are divided by the total number of pixels when AMSR-E misses. Thus, frequencies reflect how often the cloud property value occurs when precipitation is missed and together bins should add to 1. Results labeled total are calculated using all available data and results labeled seasonal are calculated by only using data from the months indicated.

Fig. 3.3 shows the range of cloud properties typical for warm clouds where AMSR-E missed warm precipitation. When AMSR-E misses precipitation, greater than 65% of misses occur for LWP from 150-400 g/m^2, $\sim$ 70% for r_e between 18 and 28 μm, greater

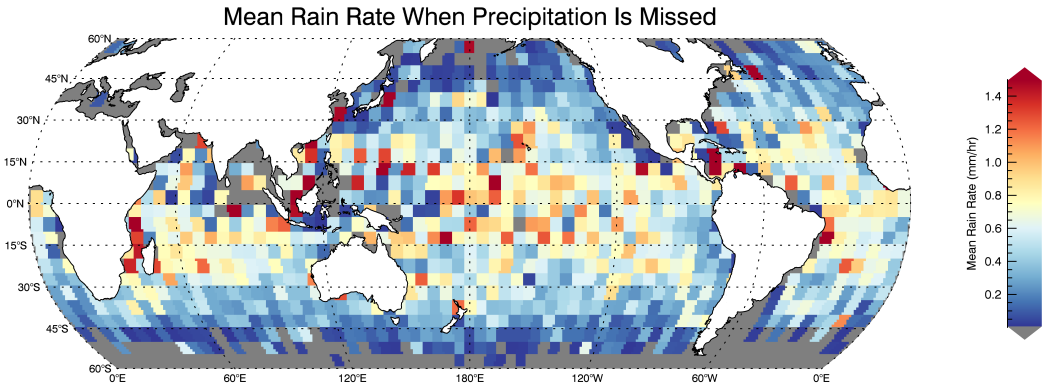

Figure 3.2: Map of global mean rain rates when AMSR-E misses precipitation and RF = 100.

than 65% for optical thicknesses between 10 and 30, and $\sim$ 70% for CTH less than 2.5 km. There is little seasonal variability in the frequency of cloud properties when precipitation is missed. Frequencies of 0 for CTHs less than 1 km in Fig. 3.3d are most likely due to a lack of CPR precipitation retrieval because of surface clutter contamination; however, Rapp et al. (2013) suggest this is a relatively infrequent occurrence. These figures suggest that the greatest improvement in the detection of AMSR-E missed precipitation should focus on moderate LWP and optical thicknesses, $r_e > 16$ μm, CTH between 1.5 and 3 km.

Together with cloud property frequencies when precipitation is missed, frequencies of missed precipitation for specific cloud properties can give additional insight into which properties would best improve warm rain detection. A histogram of value dependent frequencies of missed warm precipitation within a given cloud property range is shown in Fig. 3.4. Each histogram bin is calculated by dividing the number of pixels within a cloud property bin where AMSR-E misses precipitation by the total number of pixels where CloudSat detects precipitation for that cloud property bin. Thus, frequencies reflect the occurrence of AMSR-E misses given an observed cloud property bin. Analysis of Fig.

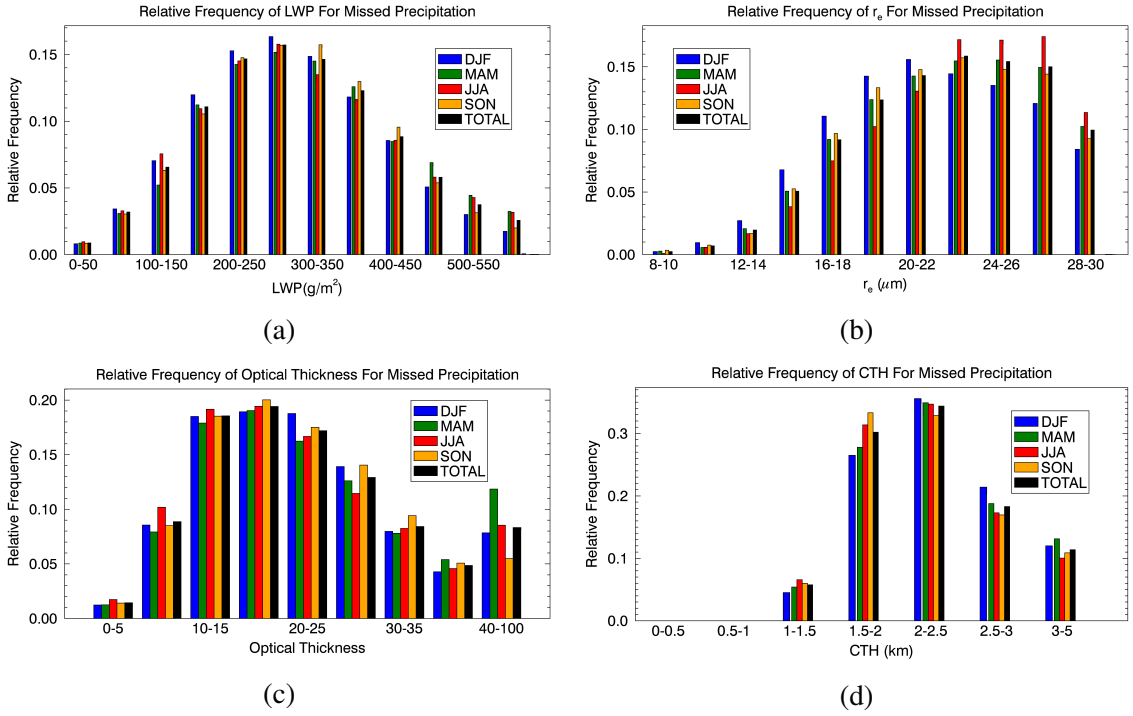

Figure 3.3: Seasonal and total relative frequencies of MODIS **(a)** LWP, **(b)** r_e, **(c)** τ, and **(d)** CloudSat-CALIPSO CTH when AMSR-E misses precipitation.

3.4 shows that missed warm precipitation is most frequent for lower LWPs, CTHs, and τ, and higher r_e. As LWP increases the frequency of AMSR-E misses tends to decrease. CTH and τ are analogous to LWP with the frequency of AMSR-E misses decreasing as values increase. r_e has an inverse relationship with AMSR-E misses, increasing as values increase. For LWP between 50 and 100 g/m^2, 150 and 200 g/m^2, CTH less than 2 km, and optical thicknesses between 5 and 10, precipitation is missed more than 40% of the time. Also, with a CTH between 1 and 1.5 km, precipitation is missed greater than 80% of the time. Clouds with a LWP between 0 and 450 g/m^2, τ between 35 and 40 and less than 25, CTH less than 2.5 km, or r_e between 16 and 28 μm have precipitation missed greater than 20% of the time. Fig. 3.4 suggests that warm rain detection biases occur frequently in low LWPs, optical thicknesses, and CTHs, and $r_e > 16$ μm.

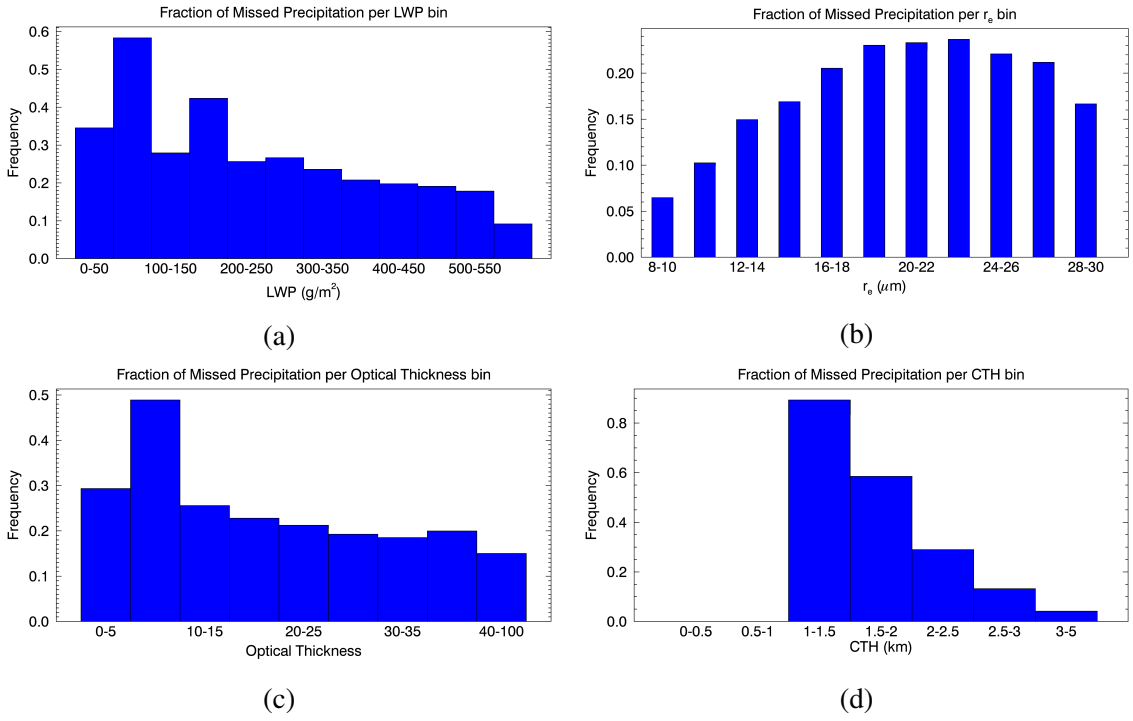

Figure 3.4: Frequency of missed AMSR-E precipitation relative to the total number of precipitating clouds per **(a)** LWP, **(b)** r_e, **(c)** τ, and **(d)** CTH bin.

Comparing Figures 3.3 and 3.4 help locate the best cloud property ranges for possible precipitation detection improvements. Warm rain detection biases occur more frequently within lower LWP, τ, and CTH bins, but biases at higher values of these properties contribute more to the total frequency of missed precipitation. Warm rain detection biases occur more frequently and biases contribute to more of the total frequency of missed precipitation for $r_e > 16$ μm. These findings suggest that AMSR-E warm rain detection biases vary as a function of the cloud properties and indicate that a priori cloud property information could help improve GPROF retrievals.

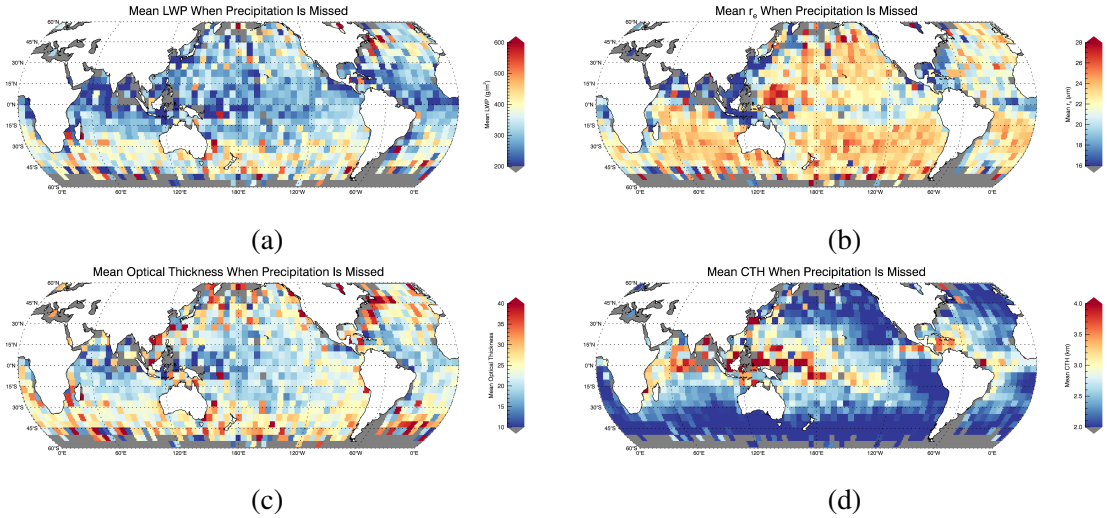

Figure 3.5: Map of global mean **(a)** LWP, **(b)** r_e, **(c)** τ, and **(d)** CTH when AMSR-E misses precipitation and RF = 100.

3.2 Global Mean Cloud Properties

Now that precipitation misses are calculated for each cloud property, the next step is to observe the spatial distribution of the cloud properties for missed precipitation and, thus, better understand where and in which cloud regimes improvements can possibly be made. Figures 3.3 and 3.4 display the frequency of cloud properties for missed precipitation. By mapping mean values of cloud properties when precipitation is missed, we can better determine which regions show the cloud macrophysical and microphysical characteristics where precipitation is missed most often. Fig. 3.5 is created by calculating the mean for each cloud property when precipitation is missed for each $5^\circ \times 5^\circ$ bin. Results show that in stratocumulus regions off the western coasts of the continents, where AMSR-E had the highest fraction of missed precipitation and CPR-observed rain rates were low, CTH is very low. Also, this cloud regime exhibits higher LWPs, r_e, and τ. In shallow cumulus and deep convective regimes, particularly the Pacific warm pool, missed precipitation occurs at higher cloud tops, low LWPs, low r_e, and low optical thicknesses. Low r_e and high optical

thicknesses off the eastern coast of the continents suggest that they might be influenced by industrial emissions (Sekiguchi et al. 2003).

Results show a distinct relationship between the four observed cloud properties and AMSR-Es warm rain detection biases. So far all four cloud properties look feasible for improving detection. A way to test the potential of cloud properties as a means of improving detection includes modifying a simplified drizzle detection method to test whether combining TBs, which are a direct measure of emission from rainfall, and cloud properties could potentially lead to improvements.

3.3 Cloud Properties vs. Brightness Temperature

To better evaluate the potential of cloud properties to improve detection, TBs and cloud properties are analyzed together. Investigating the correlations between TBs and cloud properties may show if possible thresholds can be implemented to better improve detection. In the absence of ice, TB is a direct measure of emission from liquid hydrometeors in the observed footprint. Cloud properties are plotted vs TB and results are shown in Fig. 3.6. Data for all observed warm clouds (both precipitating and non-precipitating) are plotted. Contours of detected rain and missed rain are then overlaid. The horizontally polarized 36 GHz channel was used in Fig. 3.6, but both polarizations of the 36 GHz and 89 GHz channels were analyzed. Fig. 3.6 shows a strong correlation between TBs and cloud properties. There is a noticeable offset between detected warm precipitation and missed warm precipitation for 36 GHz TBs as a function of cloud property. This offset allows for an empirically-derived curve fit threshold that could be used to include detected warm precipitation and a high concentration of missed warm rain. Fig. 2.4 showed an example of these empirically-derived curves. Similar to Miller and Yuter (2013), a threshold could be applied to the plots in Fig. 3.6 to help separate raining from non-raining cases while

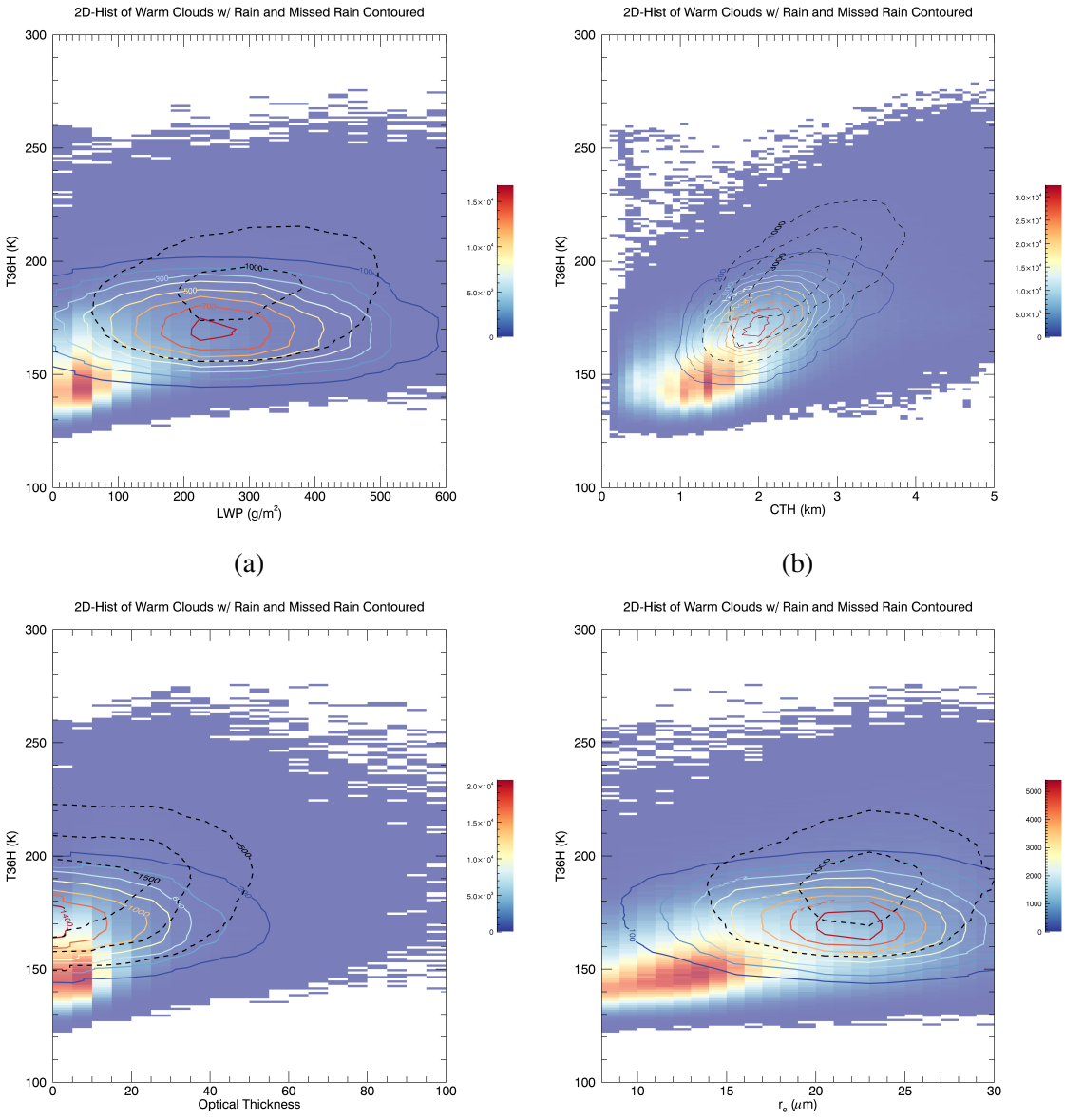

Figure 3.6: 2-D histogram of 36H GHz TB vs. **(a)** LWP, **(b)** r_e, **(c)** τ, and **(d)** CTH for all warm clouds and all RF. Colored contours indicate areas of missed warm rain and black dashed contours indicate areas of detected warm rain.

also trying to capture as much missed precipitation as possible. The threshold curves in Fig. 2.4 use a target missed precipitation fraction to perform a linear regression using a polynomial fit. The target missed precipitation fraction is systematically increased to try and capture the highest frequency of missed precipitation without adding too many false alarms. All plots in Fig. 3.6 display a feasible case for a threshold to be applied. These thresholds can be tested against current threshold methods and statistically compared to see if cloud property dependent TB thresholds can better detect warm precipitation, while limiting the additional detection errors.

3.4 Threshold Results and Comparisons

Fig. 3.6 shows that a curved fit threshold could be derived to separate the dashed contour raining pixels from the non-raining pixels. Similar to Miller and Yuter (2013), the threshold can be shifted to capture a large amount of missed precipitation without capturing too many non-raining pixels. Cloud property dependent TB thresholds are calculated by modifying a simplified drizzle detection method by Miller and Yuter (2013). A main goal of this study is to determine if additional cloud property information can be used to improve the detection of warm precipitation by the current AMSR-E GPROF algorithm and other established precipitation onset thresholds. Precipitation onset thresholds include the 89 GHz TB threshold in Miller and Yuter (2013), a simple 180 g/m^2 LWP threshold implemented by Remote Sensing Systems (RSS) (Wentz 1997), and 15μm threshold used by many previous studies. Miller and Yuter (2013) created a curve fit between cloud-free 89 GHz TBs and IWV values that was adjusted to separate a local maximum of AMSR-E LWP values greater than 200 g/m^2 from the cloud-free values. After other refinements to

the curve were made, the final threshold equation was

$$T_{89H,threshold} = -0.008875(IWV)^2 + 1.542(IWV) + 220 \tag{3.1}$$

where $T_{89,threshold}$ is the threshold value in K and IWV is the vertically integrated water vapor value in kg m^{-2}. Their threshold was originally created only for stratocumulus regimes; however, the detection statistics and results shown in Table 3.1 are computed by applying the threshold to all warm clouds for our dataset. Wentz (1990) analyzed 38 northeast Pacific storm systems and found LWPs $>$ 180 g/m^2 likely indicate drizzle. Thus, Wentz (1997) uses a LWP threshold of 180 g/m^2 to determine precipitation. Albrecht (1989) found that increases in cloud condensation nuclei (CCN) concentration lead to decreases in mean particle droplet size and drizzle production. Also, $r_e \geq 15$ μm were observed in shallow, warm cumulus that had low concentrations of CCN. Rosenfeld and Gutman (1994) compared Advanced Very High Resolution Radiometer (AVHRR) retrieved cloud top properties with ground radar data and showed that r_e greater than 14 μm matched well with areas that did have radar echoes, and thus deemed to be precipitating. For this study 15 μm was used as the precipitation onset threshold to compare against. To determine if cloud property information can improve detection, current algorithm and threshold detection statistics are calculated for comparison. Statistics are calculated for the current AMSR-E GPROF algorithm (Kummerow et al. 2001), Miller and Yuter (2013) TB threshold, RSS LWP threshold, and 15 μm r_e threshold, and are shown in Table 3.1. GPROF has reasonable skill scores and a high OR, but has a bias significantly less than one. Also, GPROF only captures 32% of precipitation occurrences, 67% of total rain volume, and has a FAR of 1%. Table 3.1 shows that the threshold created by Miller and Yuter (2013) and 15 μm r_e threshold both have low skill scores while the 180 g/m^2 RSS LWP threshold has a high skill score. All three of these thresholds have relatively high biases,

which suggests that they predict precipitation significantly more often than it occurs. They have high HRs, but at the expense of larger FARs. However, higher FARs may be acceptable if skill score is high, HR is substantially improved, and a larger amount of total precipitation is captured. Cloud property dependent TB thresholds are compared to Table 3.1, and the best results will be defined by thresholds with HRs higher than GPROF and FARs lower than RSS.

Table 3.1: GPROF and other commonly used precipitation onset thresholds

	AMSR-E GPROF	Miller and Yuter	RSS LWP (180 g/m^2)	r_e (15 μm)
HSS	0.40	0.21	0.49	0.17
CSI	0.28	0.19	0.37	0.17
OR	32.86	6.12	26.40	15.91
Bias	0.46	3.18	1.66	5.10
HR *(RF=100)*	32% *(54%)*	66% *(79%)*	72% *(90%)*	91% *(94%)*
FAR	1 %	24%	9%	41%
VHR *(RF=100)*	67% *(75%)*	86% *(89%)*	93% *(96%)*	93% *(94%)*

3.4.1 r_e

The presence of large droplets has been associated with precipitation and warm rain detection biases occur for $r_e > 16$ μm. R_e-dependent 36 GHz TB thresholds are created, while detection statistics are calculated and compared with Table 3.1. Table 3.2 shows results for a r_e-dependent 36 GHz TB threshold. Other frequencies and polarizations were also tested. Skill scores are high and ORs are moderate, but are lower than RSS. Biases indicate that precipitation is predicted less often than it occurs until at target fraction of

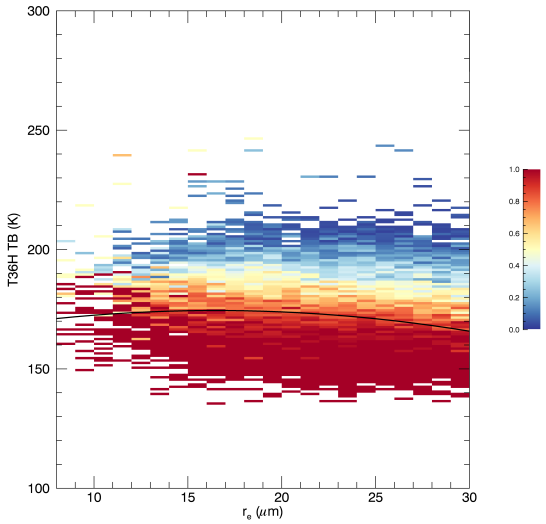

Figure 3.7: 2-D histogram of 36H GHz TB vs. r_e with missed AMSR-E precipitation fraction plotted and target fraction of 0.85 used. Solid black line indicates threshold created.

0.75. Skill scores are similar to GPROF, but higher as target fraction is increased, and are much higher than both Miller and Yuter (2013) and $r_e > 15$ μm. HRs and FARs are above GPROF, but FARs stay below RSS up until a target fraction of 90%. HRs and VHRs are shown to increase as the fraction target is increased, but FARs increase as well. HRs and VHRs for RF=100 dataset show the best detection that could be achieved if beam-filling was not an issue. A target fraction of 85% shows the best results as HR and VHR are significantly improved above GPROF while keeping FAR equivalent to RSS, and is shown in Fig 3.7. The equation for this threshold is:

$$TB36H_{threshold} = -0.0473104(r_e)^2 + 1.55737(r_e)) + 161.646 \tag{3.2}$$

where $TB36H_{threshold}$ is threshold value in K and r_e values are in μm.

Table 3.2: r_e-dependent TB threshold results

	r_e									
TB	36H	36H	36H	36H	36H	36H	36H	36H	36H	36H
Fraction Target	50%	55%	60%	65%	70%	75%	80%	85%	90%	95%
HSS	0.41	0.42	0.43	0.44	0.45	0.43	0.43	0.39	0.37	0.36
CSI	0.29	0.30	0.31	0.32	0.33	0.32	0.32	0.29	0.28	0.28
OR	25.39	24.38	21.26	20.53	21.83	17.41	16.84	13.44	13.10	14.20
Bias	0.56	0.61	0.74	0.83	0.82	1.05	1.22	1.58	1.96	2.20
HR	35%	37%	41%	45%	45%	50%	54%	59%	66%	71%
(RF=100)	*(57%)*	*(59%)*	*(64%)*	*(67%)*	*(67%)*	*(71%)*	*(75%)*	*(78%)*	*(83%)*	*(86%)*
FAR	2%	2%	3%	3%	3%	5%	6%	9%	12%	14%
VHR	71%	73%	77%	80%	80%	83%	86%	88%	91%	93%
(RF=100)	*(79%)*	*(80%)*	*(84%)*	*(86%)*	*(86%)*	*(88%)*	*(90%)*	*(92%)*	*(94%)*	*(96%)*

3.4.2 τ

Table 3.3: τ-dependent TB threshold results

	τ									
TB	36H	36H	36H	36H	36H	36H	36H	36H	36H	36H
Fraction Target	50%	55%	60%	65%	70%	75%	80%	85%	90%	95%
HSS	0.39	0.42	0.44	0.43	0.44	0.44	0.43	0.42	0.42	0.37
CSI	0.27	0.29	0.31	0.31	0.32	0.32	0.32	0.31	0.32	0.29
OR	30.28	27.45	23.86	24.00	22.66	19.76	16.69	15.79	16.59	14.59
Bias	0.46	0.56	0.68	0.68	0.76	0.91	1.17	1.36	1.55	2.12
HR	31%	35%	40%	40%	43%	47%	53%	57%	62%	70%
(RF=100)	*(54%)*	*(59%)*	*(63%)*	*(63%)*	*(66%)*	*(69%)*	*(74%)*	*(77%)*	*(81%)*	*(85%)*
FAR	1%	1%	2%	2%	3%	4%	6%	7%	9%	14%
VHR	71%	75%	78%	78%	80%	83%	86%	88%	89%	91%
(RF=100)	*(78%)*	*(82%)*	*(84%)*	*(85%)*	*(86%)*	*(89%)*	*(91%)*	*(92%)*	*(92%)*	*(93%)*

Optically thick clouds are associated with precipitation and warm rain detection biases occur for moderate τ. τ-dependent 36 GHz TB thresholds are created, while detection statistics are calculated and compared with Table 3.1. Table 3.3 shows results for a τ-dependent 36 GHz TB threshold. Other frequencies and polarizations were also tested. Skill scores and ORs are high, but skill score is lower than RSS. Biases indicate that for

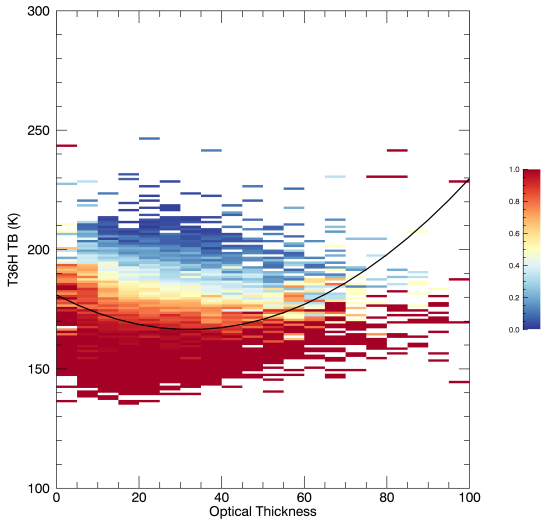

Figure 3.8: 2-D histogram of 36H GHz TB vs. τ with missed AMSR-E precipitation fraction plotted and a target fraction of 0.9 used. Solid black line indicates threshold created.

target fractions below 80% precipitation is predicted less often than it occurs. Skill scores are similar to GPROF, but higher as target fraction is increased, and higher than both Miller and Yuter (2013) and $r_e > 15$ μm. Also, ORs are much lower as target fraction is increased. τ has the lowest starting HR of all the cloud properties, but its best threshold has the highest HR of all the cloud properties. HRs and FARs are above GPROF after a target fraction of 55%, but FARs stay below RSS up until a target fraction of 95%. HRs and VHRs are shown to improve as the fraction target is increased, but FARs increase as well. A target fraction of 90% shows the best results as HR is increased $\sim$ 30% above GPROF and VHR is increased $\sim$ 22%, while keeping FAR equivalent to RSS, and is shown in Fig 3.8. The equation for this threshold is:

$$TB36H_{threshold} = 0.0138362(\tau)^2 + (-0.895954(\tau)) + 180.970 \tag{3.3}$$

where TB36H$_{threshold}$ is threshold value in K and τ values are unitless.

3.4.3 CTH

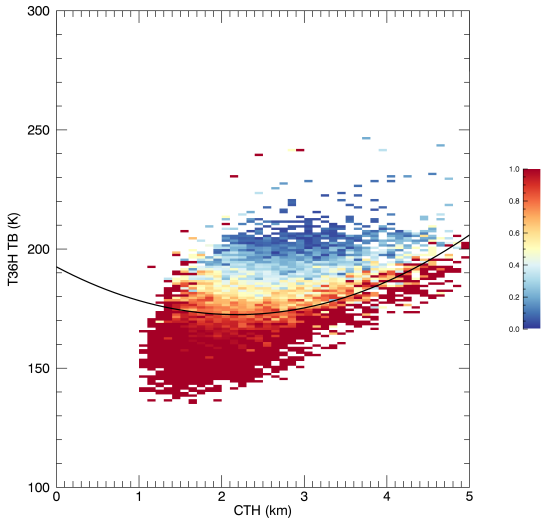

Figure 3.9: 2-D histogram of 36H GHz TB vs. CTH with missed AMSR-E precipitation fraction plotted and a target fraction of 0.85 used. Solid black line indicates threshold created.

Higher cloud tops are associated with precipitation and warm rain detection biases occur for mostly CTH less than 2.5 km. CTH-dependent 36 GHz TB thresholds are created, while detection statistics are calculated and compared with Table 3.1. Other frequencies and polarizations were also tested. Table 3.4 shows results for a CTH-dependent 36 GHz TB threshold. Skill scores are high, but lower than RSS, and ORs are lower than GPROF, RSS, and other cloud properties. Biases indicate that precipitation is predicted less often than it occurs until a target fraction of 0.75. CTH has a high starting HR, but as target fraction is increased HR and VHR are the lowest of all the cloud properties. HRs and

Table 3.4: CTH-dependent TB threshold results

	CTH									
TB	36H	36H	36H	36H	36H	36H	36H	36H	36H	36H
Fraction Target	50%	55%	60%	65%	70%	75%	80%	85%	90%	95%
HSS	0.40	0.41	0.42	0.43	0.43	0.42	0.41	0.40	0.37	0.35
CSI	0.28	0.29	0.30	0.31	0.32	0.31	0.31	0.30	0.28	0.27
OR	22.89	21.35	20.44	20.18	18.47	15.84	15.12	14.38	12.83	12.67
Bias	0.59	0.64	0.72	0.78	0.92	1.19	1.28	1.41	1.87	2.16
HR	35%	37%	40%	42%	46%	52%	54%	56%	64%	68%
(RF=100)	*(56%)*	*(58%)*	*(61%)*	*(64%)*	*(67%)*	*(72%)*	*(74%)*	*(75%)*	*(81%)*	*(83%)*
FAR	2%	2%	3%	3%	4%	6%	7%	8%	12%	14%
VHR	71%	72%	75%	78%	81%	84%	85%	86%	89%	90%
(RF=100)	*(78%)*	*(79%)*	*(82%)*	*(84%)*	*(86%)*	*(89%)*	*(90%)*	*(90%)*	*(92%)*	*(93%)*

FARs are above GPROF, but FARs stay below RSS up until a target fraction of 90%. A target fraction of 85% shows the best results as HR is increased significantly from GPROF while decreasing FAR just below RSS, and is shown in Fig 3.9. When the CTH-dependent TB threshold is applied to the RF = 100 dataset, HR and VHR are increased to 75% and 90%, respectively. The equation for this threshold is:

$$TB36H_{threshold} = 4.20960(CTH)^2 + (-18.3734(CTH)) + 192.517 \tag{3.4}$$

where TB36H$_{threshold}$ is threshold value in K and CTH values are in km.

3.4.4 LWP

Higher LWPs are associated with precipitation and warm rain detection biases occur for moderate LWPs. LWP-dependent 36 GHz TB thresholds are created, while detection statistics are calculated and compared with Table 3.1. Other frequencies and polarizations were also tested. Table 3.5 shows results for a LWP-dependent 36 GHz TB threshold. LWP skill scores become similar to RSS and are much higher than GPROF, Miller and Yuter (2013), and r$_e$ $>$ 15 μm as target fraction is increased. LWP has the highest skill

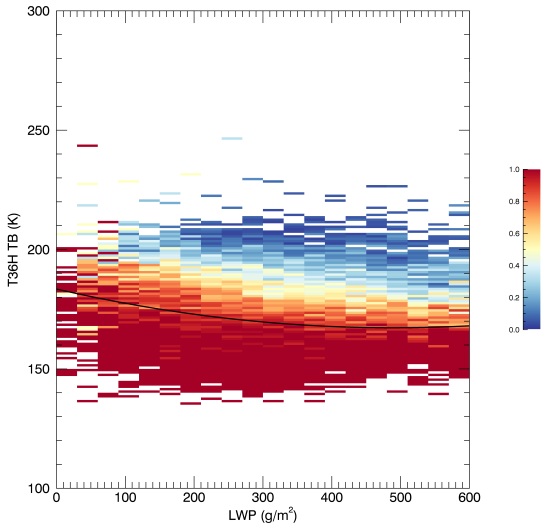

Figure 3.10: 2-D histogram of 36H GHz TB vs. LWP with missed AMSR-E precipitation fraction plotted and a target fraction of 0.9 used. Solid black line indicates threshold created.

scores and ORs of all the cloud properties. Biases indicate that precipitation is predicted less often than it occurs for target fractions lower than 85%. FARs stay below RSS for all target fractions, but VHR actually decreases for a target fraction of 95%. When the LWP-dependent threshold is applied to the RF = 100 dataset, VHR also decreases for a target fraction of 95%. A target fraction of 90% shows the best results as HR is increased significantly from GPROF, VHR is maximized, and FAR is held just below RSS, and it is shown in Fig 3.10. The equation for the 90% target fraction threshold is:

$$TB36H_{threshold} = 6.77347e^{-5}(LWP)^2 + (-0.0663133(LWP)) + 183.443 \qquad (3.5)$$

where TB36H$_{threshold}$ is threshold value in K and LWP values are in g/m^2.

Table 3.5: LWP-dependent TB threshold results

	LWP									
TB	36H	36H	36H	36H	36H	36H	36H	36H	36H	36H
Fraction Target	50%	55%	60%	65%	70%	75%	80%	85%	90%	95%
HSS	0.41	0.42	0.43	0.45	0.47	0.48	0.48	0.48	0.47	0.46
CSI	0.28	0.29	0.31	0.32	0.34	0.35	0.36	0.35	0.35	0.35
OR	37.54	35.11	25.35	31.93	29.19	27.81	25.38	22.35	20.66	20.78
Bias	0.44	0.48	0.64	0.59	0.70	0.76	0.87	1.05	1.26	1.45
HR	32%	33%	39%	39%	44%	46%	49%	54%	59%	64%
(RF=100)	*(56%)*	*(58%)*	*(63%)*	*(64%)*	*(68%)*	*(71%)*	*(73%)*	*(76%)*	*(79%)*	*(81%)*
FAR	1%	1%	2%	2%	2%	3%	3%	5%	6%	8%
VHR	72%	73%	79%	77%	81%	84%	84%	86%	88%	86%
(RF=100)	*(81%)*	*(81%)*	*(86%)*	*(83%)*	*(87%)*	*(90%)*	*(89%)*	*(91%)*	*(91%)*	*(88%)*

3.4.5 Best Results

All cloud property dependent TB thresholds showed promising results, as summarized in Table 3.6. All cloud properties produced similar HRs and VHRs compared to Miller and Yuter (2013) and $r_e > 15$ μm, and FARs were noticeably lower. Also, all cloud properties produced more hits and captured more rain volume than GPROF. Some false alarms were added compared to GPROF, but HRs and VHRs were increased significantly, and FARs stayed below or at RSS's 9%. When compared against one another τ and LWP have some noticeable advantages. τ produces a higher HRs and VHRs than the other properties. Also, when cloud property dependent thresholds are applied to the RF = 100 dataset, τ has a higher HR and VHR. While exhibiting a lower, but similar HR and VHR than τ, LWP exhibits a higher skill score, larger OR, and a lower FAR. Maximizing VHR may be considered one the most important goals, and while τ exhibits the largest VHR, all other cloud properties are similar.

Since these results show that using cloud property information can help in the detection of warm precipitation, HR and FAR differences are plotted globally. Figure 3.11 shows HR and FAR differences between AMSR-E GPROF and LWP dependent 36H GHz

Table 3.6: Best threshold results

	r_e	τ	CTH	LWP
TB	36H	36H	36H	36H
Fraction Target	85%	90%	85%	90%
HSS	0.39	0.42	0.40	0.47
CSI	0.29	0.32	0.30	0.35
OR	13.44	16.59	14.38	20.66
Bias	1.58	1.55	1.41	1.26
HR	59%	62%	56%	59%
(RF=100)	*(78%)*	*(81%)*	*(75%)*	*(79%)*
FAR	9%	9%	8%	6%
VHR	88%	89%	86%	88%
(RF=100)	*(92%)*	*(92%)*	*(90%)*	*(91%)*

TB threshold to help determine the regions where improvements can be made. Calculated HRs and FARs for AMSR-E and the LWP-dependent 36H GHz TB threshold are averaged for each $5^\circ \times 5^\circ$ bin and the AMSR-E GPROF results are subtracted from LWP-dependent TB threshold results. Figures 3.11a and 3.11b show that the use of cloud property information can help improve warm rain HRs in the tropics and Indo-Pacifc warm pool, where shallow cumulus and mostly deep convection are found, for the LWP dependent 36H GHz TB threshold. However, the addition of cloud property information shows little to no improvement of HRs in stratocumulus regions where warm rain is prominent. In the tropics, where HRs are improved, FARs are also increased. Also, slight increases of FAR are seen in stratocumulus regimes. These results suggests that the addition of LWP information does not necessarily improve hit rates in stratocumulus regions, but does help better detect warm rain in regions most associated with shallow cumulus and deep convection. A similar pattern is seen for all other cloud property dependent thresholds. Together they provide results that vary depending on region, and thus improvements to thresholds might occur if stratified by different environmental and cloud regimes.

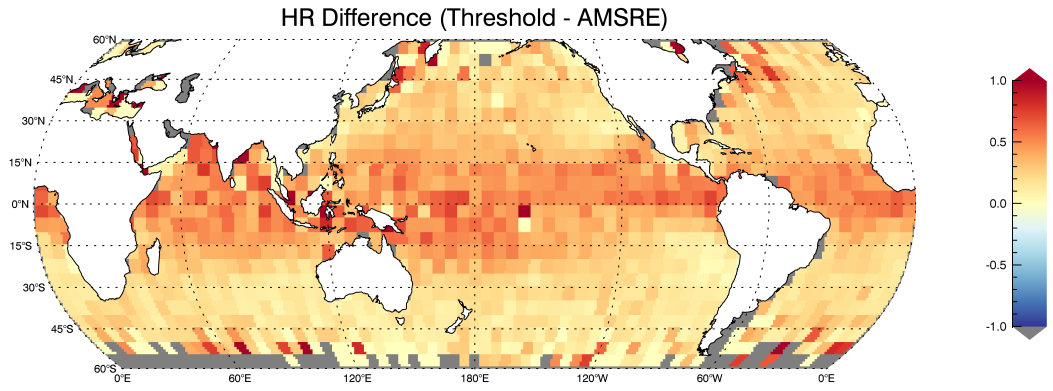

(a)

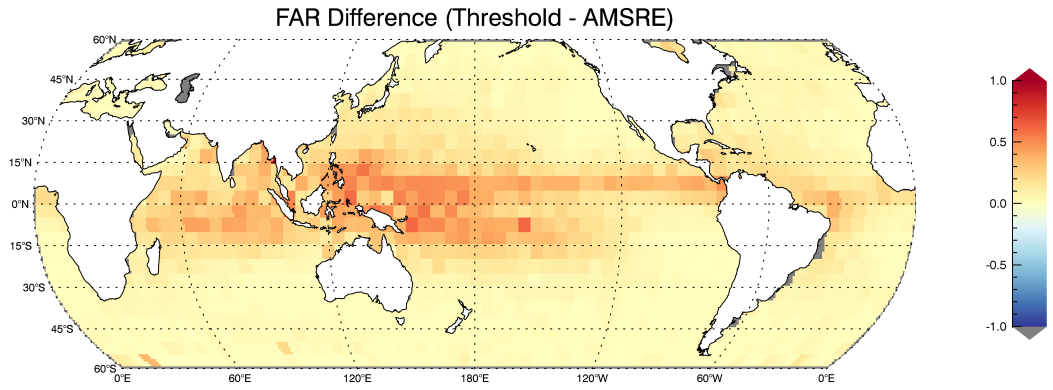

(b)

Figure 3.11: Global **(a)** HR and **(b)** FAR differences between AMSR-E GPROF and LWP dependent 36H GHz TB threshold.

3.5 Regime Dependent Thresholds

Cloud property dependent TB thresholds are applied to the entire globe and the improvement of HRs and FAR can vary regionally as seen in Figure 3.11. Fig. 3.10 shows that, depending on the region and cloud morphology, the threshold does not always work. Regime specific cloud property dependent TB thresholds are tested within different cloud

regimes to determine whether detection statistics can be improved. Data is partitioned by environmental and cloud regimes, and then thresholds are calculated similar to the process discussed in section 2.4.4, but the data is constrained to particular environmental characteristics to define specific environmental and cloud regimes.

3.5.1 Dynamical Regimes

TBs are dependent upon the amount of energy received by the PMW sensor, and so thresholds will benefit from clouds that produce large areas of heavier precipitation. Large scale ascent regimes are associated with deeper convective systems and other cumuliform clouds that produce larger rain rates and a stronger emission signal (Bony et al. 2004). Large scale subsidence regimes are associated with a large fraction of stratocumulus clouds and other low-level boundary layer clouds that, while they are widespread, have very low rain rates and produce a weaker emission signal (Bony et al. 2004). Also, a smaller amount of shallow cumulus clouds can be associated with subsidence regimes, and they can produce larger rain rates, but these smaller cells are isolated. When determining if environmental and cloud regimes can improve cloud property dependent TB thresholds, we would expect that constraining the data by dynamical regimes might improve thresholds due to a larger fraction of signatures that produce a larger emission signal. Ascent and subsidence regimes are separated by using 500 hectopascal (hPa) vertical velocity (ω) thresholds as a proxy for large scale ascending and descending motions as in Bony and Dufresne (2005). Six-hourly 500 hPa ω data is from European Centre for Medium-Range Weather Forecasts (ECMWF) ERA-Interim reanalysis data (Dee et al. 2011). Data with ω values less than 0 indicates an ascent regime and ω values greater than 0 indicate a subsidence regime. Cloud property dependent TB thresholds are calculated for both regimes. Also, the best thresholds, shown in Table 3.6, are applied to the constrained data and compared with regime threshold results to determine if improvements are made. Results for

the global thresholds applied to dynamical regime-dependent data are shown in Table 3.7. Results for ascent regimes are shown in Table 3.8, and results for subsidence regimes are shown in Table 3.10.

Results show that improvements to cloud property dependent TB threshold HRs can be

Table 3.7: Global thresholds applied to dynamical regimes

	r_e	τ	CTH	LWP	r_e	τ	CTH	LWP
	Ascent Regime				Subsidence Regime			
HSS	0.39	0.41	0.41	0.48	0.38	0.42	0.39	0.46
CSI	0.31	0.33	0.32	0.37	0.28	0.32	0.29	0.34
OR	13.65	19.67	14.32	20.31	13.46	19.39	14.50	21.20
Bias	1.87	2.15	1.65	1.50	1.43	1.82	1.27	1.13
HR	68%	79%	65%	68%	54%	68%	51%	54%
(RF=100)	*(85%)*	*(92%)*	*(82%)*	*(85%)*	*(74%)*	*(87%)*	*(71%)*	*(75%)*
FAR	13%	16%	11%	9%	8%	10%	6%	5%
VHR	92%	97%	90%	91%	85%	94%	83%	85%
(RF=100)	*(95%)*	*(98%)*	*(93%)*	*(93%)*	*(90%)*	*(97%)*	*(88%)*	*(89%)*

made if data is constrained by descent regimes. r_e shows the biggest improvements in HR and VHR (RF=100 statistics as well) at the expensive of only adding 2% to the FAR. The 95% target fraction LWP threshold was considered the best result since it did not increase FAR above RSS, but the significant increase in HR and VHR allowed the 90% target fraction r_e threshold to be chosen. In ascent regimes, all cloud properties significantly decreased FARs, but they did not see improvements from ascent-dependent thresholds as HRs and VHRs decreased. In subsidence regimes LWP, r_e, and CTH-dependent thresholds improve warm rain detection. LWP and r_e increase both HR and VHR, while CTH only increases HR. In ascent regimes, all cloud properties failed to make any improvements. Results show that in regions where warm rain is prominent, a regime-dependent cloud property-dependent threshold can improve warm rain detection. This is most likely due

Table 3.8: Ascent regimes

	r_e	τ	CTH	LWP
TB	36H	36H	36H	36H
Fraction Target	80%	80%	75%	75%
HSS	0.46	0.45	0.42	0.51
CSI	0.35	0.34	0.32	0.39
OR	17.56	16.24	13.70	24.56
Bias	1.45	1.40	1.44	0.94
HR *(RF=100)*	64% *(83%)*	62% *(81%)*	60% *(78%)*	54% *(77%)*
FAR	9%	9%	9%	4%
VHR *(RF=100)*	90% *(94%)*	90% *(94%)*	86% *(91%)*	88% *(92%)*

to the low rain rates that are prominent in subsidence regimes that cause TBs to be lower, which can be accounted for in regime-dependent thresholds. In regions with deeper convection, results suggest that regime-dependent thresholds do not improve detection over the global cloud property-dependent thresholds. Results show that τ does not see any improvements with dynamical regime dependent thresholds. LWP, r_e, and CTH-dependent horizontally polarized 36 GHz TB thresholds exhibit the most promising results in descent regimes. Thresholds are shown in Fig. 3.12 and the equations for these thresholds are:

$$TB36H_{threshold} = -0.00103199(r_e)^2 + (-0.177245)(r_e) + 174.437 \tag{3.6}$$

$$TB36H_{threshold} = 11.3531(CTH)^2 + (-49.5681)(CTH) + 221.980 \tag{3.7}$$

$$TB36H_{threshold} = 6.91527e-05(LWP)^2 + (-0.0601593)(LWP) + 179.610 \tag{3.8}$$

where $TB36H_{threshold}$ is threshold value in K and r_e values are in μm, CTH values are in km, and LWP values are in g/m^2. Next, this process is repeated and thresholds are examined for cloud regimes.

Table 3.9: Subsidence regimes

	r_e	τ	CTH	LWP
TB	36H	36H	36H	36H
Fraction Target	90%	90%	90%	95%
HSS	0.36	0.40	0.38	0.43
CSI	0.27	0.29	0.28	0.32
OR	12.73	14.93	13.18	18.26
Bias	1.70	1.54	1.51	1.39
HR *(RF=100)*	58% *(77%)*	58% *(77%)*	55% *(72%)*	58% *(77%)*
FAR	10%	8%	8%	7%
VHR *(RF=100)*	88% *(92%)*	87% *(91%)*	81% *(85%)*	86% *(90%)*

3.5.2 Stratocumulus vs. Shallow Cumulus

In section 3.5.1 we constrained the data solely by dynamical environmental characteristics. Multiple types of clouds can be found in such regimes, and so, this section will focus on adding a thermodynamic constraint to help separate of cloud regimes. The warm cloud population is mostly comprised of stratocumulus and shallow cumulus. Medeiros and Stevens (2011) used both 500 hPa ω and 700 hPa ω greater than 10 hPa day^{-1} to define low clouds. They also found that in addition to using ω, a lower tropospheric stability (LTS) threshold of 18.55 K can be used to help distinguish different low cloud regimes. Values greater than or equal to 18.55 K are generally associated with stratocumulus clouds. Values less than 18.55 K distinguish areas of shallow cumulus. LTS is calculated by taking the potential temperature at the surface and subtracting from the potential temperature at 700 hPa seen as:

$$LTS = \theta_{700hPa} - \theta_{sfc} \tag{3.9}$$

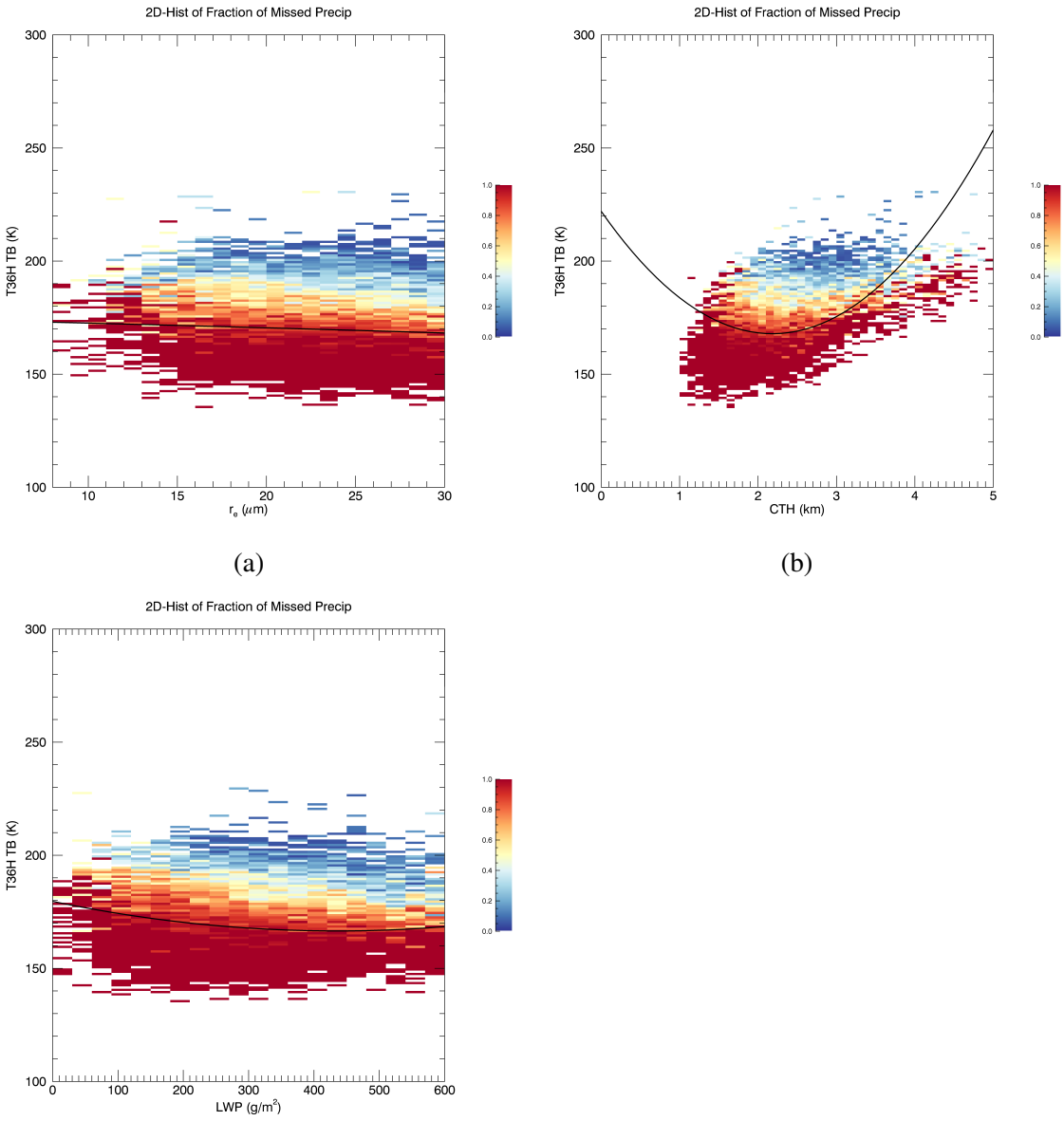

Figure 3.12: 2-D histogram of 36H GHz TB vs. **(a)** r_e (target fraction of .9), **(b)** CTH (target fraction of .9), and **(c)** LWP (target fraction of .95) with missed AMSR-E precipitation fraction plotted for descent regimes. Solid black line indicates threshold created.

where LTS, θ_{700hPa}, and θ_{sfc} are in K. Six-hourly potential temperature is from ECMWF ERA-Interim reanalysis data. A 500 hPa ω threshold is used to define low clouds by limiting data to values greater than 10 hPa day^{-1}. Results for the global thresholds applied to cloud regime-dependent data are shown in Table 3.10. Cloud property-dependent TB thresholds are calculated for both cloud regimes and results are shown in Tables 3.11 and 3.12.

The cloud regime-dependent r_e, LWP, and CTH-dependent TB thresholds show improvements when data is constrained by stratocumulus regimes. r_e shows the biggest improvements in HR and VHR (RF=100 statistics as well) at the expensive of only adding 6% to the FAR. Also, LWP and CTH saw large improvements in HR with smaller improvements in VHR. In stratocumulus regimes, τ did not see an improvement in HRs or VHRs. All four properties did not see improvements from shallow cumulus-dependent thresholds as HRs and VHRs decreased. Results suggest that in regions where warm rain is prominent, a regime-dependent cloud property-dependent threshold can improve warm rain detection. In regions with shallow cumulus, results show that regime-dependent thresholds

Table 3.10: Global thresholds applied to cloud regimes

	r_e	τ	CTH	LWP	r_e	τ	CTH	LWP
	Shallow Cumulus Regime				Stratocumulus Regime			
HSS	0.37	0.43	0.38	0.46	0.30	0.34	0.30	0.34
CSI	0.30	0.35	0.31	0.36	0.19	0.23	0.19	0.22
OR	9.77	15.85	10.45	16.00	21.60	19.16	24.55	27.34
Bias	1.61	1.84	1.44	1.24	0.69	1.67	0.57	0.68
HR	60%	73%	58%	60%	27%	50%	25%	31%
(RF=100)	*(78%)*	*(90%)*	*(76%)*	*(79%)*	*(50%)*	*(74%)*	*(46%)*	*(55%)*
FAR	13%	15%	11%	8%	1%	5%	1%	1%
VHR	87%	95%	85%	87%	66%	74%	64%	69%
(RF=100)	*(92%)*	*(98%)*	*(90%)*	*(90%)*	*(77%)*	*(92%)*	*(74%)*	*(78%)*

Table 3.11: Shallow cumulus regimes

	r_e	τ	CTH	LWP
TB	36H	36H	36H	36H
Fraction Target	85%	80%	85%	90%
HSS	0.44	0.43	0.40	0.43
CSI	0.34	0.33	0.32	0.34
OR	13.89	13.51	11.55	13.36
Bias	1.19	1.07	1.25	1.36
HR *(RF=100)*	56% *(76%)*	52% *(72%)*	55% *(73%)*	60% *(79%)*
FAR	8%	7%	9%	10%
VHR *(RF=100)*	85% *(90%)*	83% *(88%)*	83% *(88%)*	87% *(91%)*

do not improve detection and suggest that it would be better to use global cloud property-dependent thresholds. Results show that τ does not see any improvements with cloud regime dependent thresholds. CTH, r_e, and LWP dependent horizontally polarized 36 GHz TB thresholds exhibit the most promising results in stratocumulus regimes. Thresholds are shown in Fig. 3.13 and the equations for these thresholds are:

$$TB36H_{threshold} = -0.0408363(r_e)^2 + 1.93246(r_e) + 145.177 \tag{3.10}$$

$$TB36H_{threshold} = 8.67569e-05(LWP)^2 + (-0.0607493)(LWP) + 176.949 \tag{3.11}$$

$$TB36H_{threshold} = -8.97435(CTH)^2 + (-35.0792)(CTH) + 202.636 \tag{3.12}$$

where $TB36H_{threshold}$ is threshold value in K and r_e values are in μm, LWP values are in g/m^2, and CTH values are in km.

Cloud property dependent thresholds are shown to increase the detection of warm precipitation globally. LWP, r_e, and CTH-dependent TB thresholds can generally be improved for descent regimes and in stratocumulus regimes. Ascent and shallow cumulus

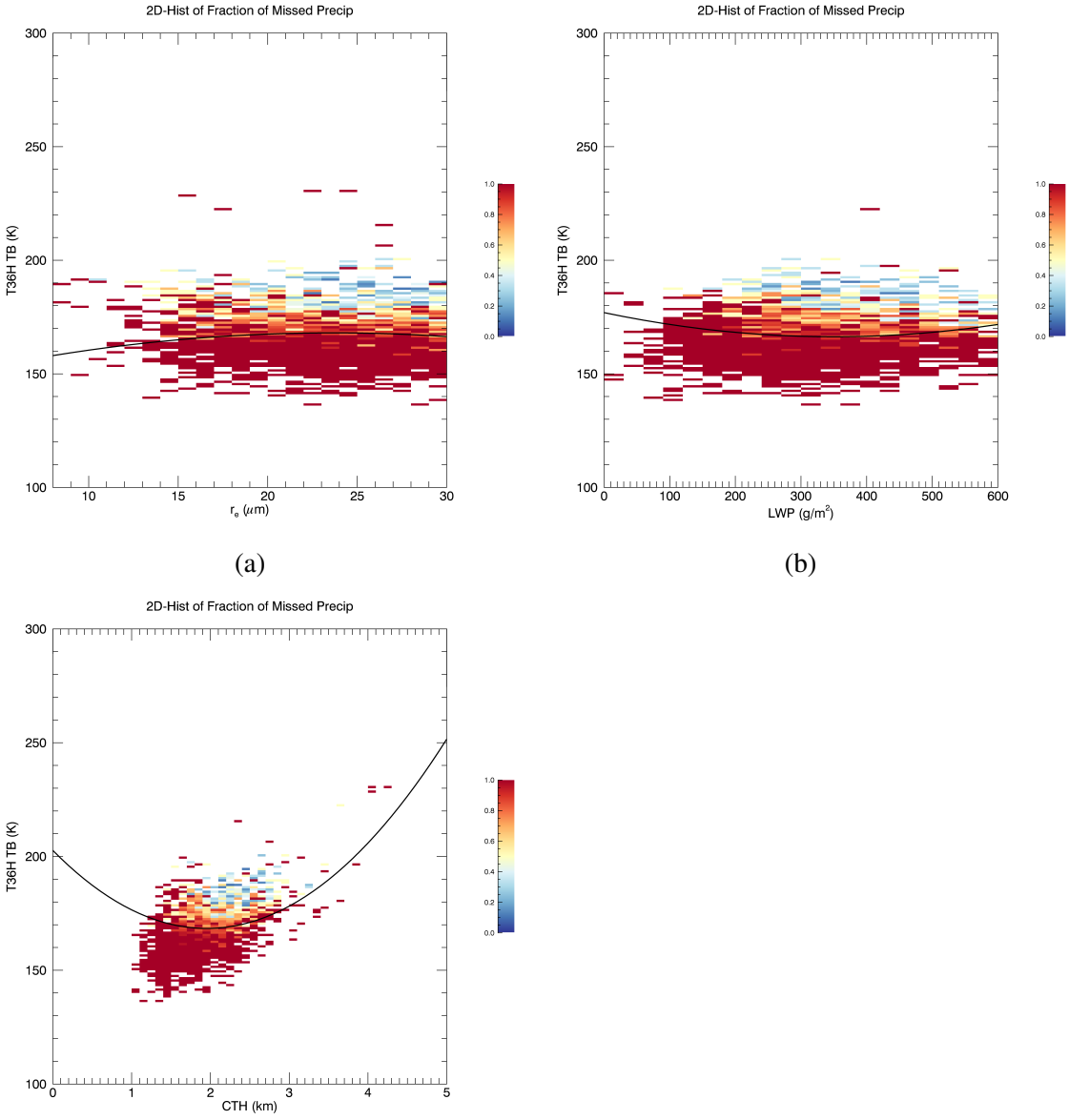

Figure 3.13: 2-D histogram of 36H GHz TB vs. **(a)** r_e (target fraction of .95), **(b)** LWP (target fraction of .95), and **(c)** CTH (target fraction of .85) with missed AMSR-E precipitation fraction plotted for stratocumulus regimes. Solid black line indicates threshold created.

Table 3.12: Stratocumulus regimes

	r_e	τ	CTH	LWP
TB	36H	36H	36H	36H
Fraction Target	95%	85%	85%	95%
HSS	0.21	0.37	0.33	0.34
CSI	0.15	0.20	0.22	0.22
OR	8.67	16.35	21.70	20.30
Bias	2.18	1.13	0.89	1.70
HR	41%	35%	34%	38%
(RF=100)	*(61%)*	*(58%)*	*(55%)*	*(58%)*
FAR	7%	3%	2%	2%
VHR	77%	74%	71%	70%
(RF=100)	*(84%)*	*(83%)*	*(79%)*	*(76%)*

regimes failed to improve TB threshold global statistics. Globally, these cloud property-dependent TB thresholds perform better than AMSR-E GPROF and are best utilized in ascent regimes, shallow cumulus regimes, and regions with deeper convection. Warm rain detection can be further improved in descent and stratocumulus regimes by utilizing regime-separated cloud property-dependent thresholds. Global cloud property-dependent thresholds perform well in regimes with upward motion and with clouds that provide a large emission signal. In regimes where warm rain is prominent and emission signals are generally weaker, detection can be improved by utilizing regime-dependent TB thresholds. All calculated cloud property-dependent TB thresholds show large increases in HRs and VHRs when thresholds are applied to only the RF = 100 data. Although it is rare for all precipitation signatures to fill the entire AMSR-E footprint, it is important to analyze RFs and determine the impact that cloud morphology has on detection results.

3.6 Rain Fraction and Precipitation Detection

In previous sections, cloud property-dependent TB thresholds were applied to the RF = ALL dataset. HRs and VHRs are significantly improved cloud property-dependent TB thresholds are applied to RF = 100 dataset. Utilizing only data where precipitation features completely fill AMSR-Es footprint would be ideal, but such a perfect case rarely occurs in nature. PMW retrievals have difficulties in detecting and measuring light precipitation in shallow clouds that do not fill the IFOV. Miller and Yuter (2013) found that based upon a study done by Lafont and Guillemet (2004), heavy drizzle was most likely to be missed by their retrieval algorithm when precipitation features comprised less than 80% of the footprint. Analyzing cloud property dependent TB thresholds where the data is constrained by RF ranges can show the lowest RF that can be used before detection is significantly affected. Cloud property dependent TB threshold results are computed as in Section 3.4. RF ranges of 15% are examined to determine how the morphology of the rain system as indicated by the RF impacts precipitation detection. Detection statistics are calculated as in the cloud property dependent horizontally polarized 36 GHz TB thresholds shown in Table 3.6 and plotted for a given RF range in Figure 3.14.

Figure 3.14 displays the change in HR, VHR, and FAR when lower RFs are added to the data. Figures 3.14a and 3.14b show a sharp decrease in HR and VHR when allowing lower RFs. As expected, both display the best warm rain detection statistics when utilizing RFs $= 100\%$. HR and VHR begin decreasing fast when allowing RF < 100. HR continually decreases when allowing lower RFs, while VHR quickly decreases for RFs $<$ 100, slows down for RFs $< 60\%$, and then sharply decreases again for RFs $< 45\%$. When allowing RFs lower than 45%, 18% lower HRs, 3% less rain volume, and $\sim 0.5\%$ increase in FAR is observed. All other cloud property dependent TB thresholds display similar results. Results are consistent with Miller and Yuter (2013) findings and suggest a higher

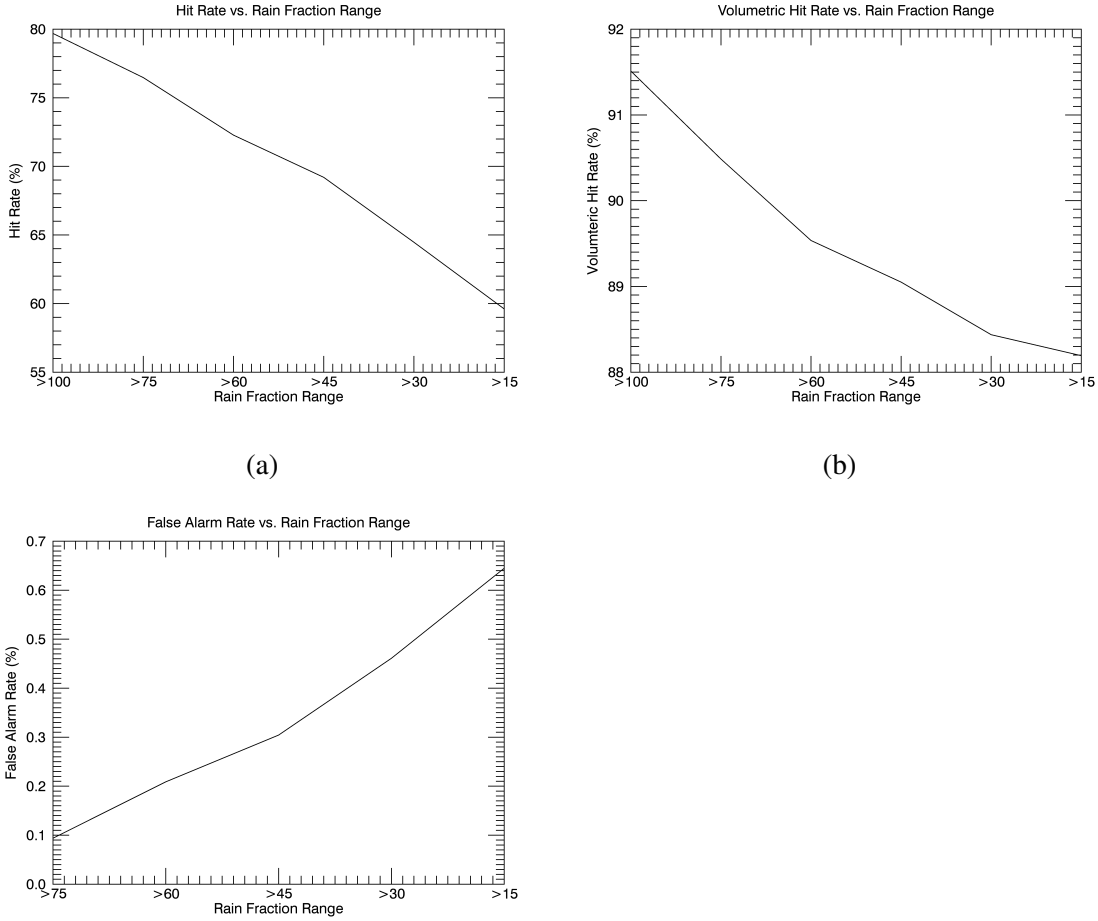

Figure 3.14: **(a)** Hit Rate, **(b)** Volumetric Hit Rate, and **(c)** False Alarm Ratio vs. RF range for LWP dependent horizontally polarized 36 GHz TB threshold (target fraction of 0.9).

fractional footprint coverage to improve warm precipitation detection.

4. SUMMARY AND CONCLUSIONS

PMW rainfall retrievals often fail to detect light, warm precipitation or have light, warm rain intensity biases because they cannot differentiate between emission from cloud and rain water. AMSR-E significantly underestimates warm rain frequency compared to CloudSat. Collocated and matched A-Train satellite observations from 2007-2009 are used to understand the relationship between cloud properties and PMW warm rain detection biases with the ultimate goal of determining the potential of cloud property information to aid in the detection of warm rain from PMW sensors. A high fraction of missed warm precipitation is seen in stratocumulus regions off the western coasts of continents where warm rain is prominent. Low mean rain rates are also found in these regions when warm precipitation is missed. The low rain rates are a big factor in the high fraction of misses because they give a weak emission signal for the PMW sensor.

Previous studies have linked LWP, CTH, r_e, and τ to the onset of precipitation and each property was examined for warm rain detection biases. Warm rain detection biases occur more frequently within lower LWP, τ, and CTH bins, but biases at higher LWP, τ, and CTH contribute more to the total frequency of missed precipitation. Missed warm rain occurs more frequently and contributes to more of the total frequency of missed precipitation for $r_e > 16$ μm. These findings suggest that AMSR-E has warm rain detection biases and it implies that a priori cloud property information could help improve GPROF retrievals. Analysis of warm rain distributions show the potential for using cloud property dependent TB thresholds to capture warm rain. Since it is beyond the scope of this study to create a new GPROF database sorted by cloud properties to test whether they help GPROF retrievals, cloud property-dependent TB thresholds were created using a technique similar to Miller and Yuter (2013) to attempt to improve warm rain detection. Cloud property-

dependent thresholds were compared to several existing methods. All cloud property dependent TB thresholds showed potential improvements, with HRs and VHRs significantly increased over AMSR-E GPROF. FARs rates were higher than AMSR-E GPROF, but promising results included FARs at or below RSS. All four cloud properties had a similar HR and VHR, but FAR was the lowest for LWP. Also, VHR was the highest for τ, which may be the most important variable since it captures more of the overall rain volume.

Cloud property dependent TB threshold HRs and VHRs varied globally, with improved HRs in regions where shallow cumulus and deeper convection is found. Little to no improvement was seen in stratocumulus regimes where warm rain is most frequently missed. Cloud property-dependent TB thresholds were investigated to determine if thresholds can be improved by constraining data to environmental and cloud regimes. ω thresholds were used to separate data into ascent and subsidence regimes. A LTS threshold, together with a ω threshold, was used to divide low clouds into two separate cloud regimes. LWP and r_e-dependent TB thresholds improved HRs and VHRs in subsidence regimes, while CTH improved HR, but not VHR. All cloud properties failed to improve over the global thresholds in ascent regimes. LWP, r_e, and CTH increased HRs and VHRs in stratocumulus regimes, but none exhibited additional improvements over the globally-driven TB thresholds in shallow cumulus regimes. In stratocumulus and subsidence regimes, where warm rain is most frequently missed, a regime-dependent TB threshold would perform best.

Results suggest that regions that generally have larger emissions signals perform best with global cloud property-dependent TB thresholds and regions that generally have weaker emission signals can be improved with regime-dependent TB thresholds. However, cloud property-dependent TB threshold results are limited by the method in which the threshold is created and are not necessarily physcial. Lower missed precipitation fractions are generally found at higher TBs and cloud property values because it becomes less likely that a cloud with higher LWPs, higher cloud tops, and larger particles does not have some

precipitation. Higher missed precipitation fractions are generally found at lower TBs and cloud property values because there is a smaller emission signal and PMW sensor have a hard time distinguishing between cloud and rain. By using target missed precipitation fractions to create these thresholds, results are skewed towards higher missed precipitation fractions and are atypical to what would be physically expected. Lower TB thresholds are seen at cloud property values where emission signals are typical stronger. This may cause the global cloud property-dependent TB thresholds to perform better in regimes with stronger emission signals.

These results suggest that aprori knowledge of cloud property information and environmental information might improve the detection of warm precipitation in PMW retrievals. With this information the next step would be to analyze the feasibility of adding cloud property information into GPROF. The difference in resolution between MODIS cloud properties and AMSR-E TB data makes it difficult to accurately portray cloud properties in the a priori database. Cloud properties can vary throughout an AMSR-E footprint and would need to be averaged to a signal value for the entire footprint. Also, r_e, τ, and LWP MODIS data is only available during the day and so diurnal variation in cloud properties would not be included. With the conclusion that cloud property information can improve the detection of warm precipitation in PMW retrievals, further studies must be conducted to determine if it can be operationally performed.

Warm precipitation biases and threshold statistics in stratocumulus regimes could be underestimated since MODIS cloud properties limits the analysis to the daytime and marine stratocumulus are found to drizzle more frequently and intensely at night (Miller and Yuter 2013). Another limitation of this study is the common beam filling error associated with PMW retrievals. Results show that when thresholds are applied to RF = 100 dataset detection is significantly improved, however CloudSat is nadir-only and thus RF $=$ 100 still does not actually sample the entire AMSR-E IFOV. Data was examined to determine

how much RF impacted warm rain detection and possibly determine a RF threshold that would limit the large addition of false alarms. Results show a significant decrease in HR and VHR when allowing lower RFs to be used. FAR is increased the most for RFs lower than 45%, along with a significant decrease in HR and VHR. Results are consistent with Miller and Yuter (2013) findings that a higher fractional footprint coverage to improve warm precipitation detection, and allowing RFs below 45% significantly decreases warm rain detection.

PMW sensors have warm precipitation detection biases that have a strong relationship with cloud properties. By using TBs combined with cloud properties, this study created cloud property-dependent TB thresholds and compared detection statistics against current GPROF detection statistics. It is shown that the addition of cloud property information into PMW rainfall retrievals could aid in the detection of warm precipitation. Also, the removal of pixels with RFs below 45% could significantly improve warm rain detection.

REFERENCES

Adler, R., T. Wilheit Jr, C. Kummerow, and R. Ferraro, 2004: Amsr-e/aqua l2b global swath rain rate/type gsfc profiling algorithm version 2. Boulder, CO: Nat. Snow and Ice Data Center.

Albrecht, B. A., 1989: Aerosols, cloud microphysics, and fractional cloudiness. *Science*, **245**, 1227–1230.

Ashcroft, P., and F. Wentz, 2006: Amsr-e/aqua l2a global swath spatially-resampled brightness temperatures, version 2.

Beard, K. V., and H. T. Ochs III, 1993: Warm-rain initiation: An overview of microphysical mechanisms. *Journal of Applied Meteorology*, **32 (4)**, 608–625.

Behrangi, A., K. Hsu, B. Imam, and S. Sorooshian, 2010: Daytime precipitation estimation using bispectral cloud classification system. *Journal of Applied Meteorology and Climatology*, **49 (5)**, 1015–1031.

Behrangi, A., M. Lebsock, S. Wong, and B. Lambrigtsen, 2012: On the quantification of oceanic rainfall using spaceborne sensors. *Journal of Geophysical Research: Atmospheres*, **117 (D20)**.

Berg, W., T. L'Ecuyer, and J. M. Haynes, 2010: The distribution of rainfall over oceans from spaceborne radars. *Journal of Applied Meteorology and Climatology*, **49 (3)**, 535–543.

Berg, W., T. L'Ecuyer, and C. Kummerow, 2006: Rainfall climate regimes: The relationship of regional trmm rainfall biases to the environment. *Journal of Applied Meteorology and Climatology*, **45 (3)**, 434–454.

Blyth, A. M., J. H. Lowenstein, Y. Huang, Z. Cui, S. Davies, and K. S. Carslaw, 2013: The production of warm rain in shallow maritime cumulus clouds. *Quarterly Journal of the*

Royal Meteorological Society, **139 (670)**, 20–31.

Bony, S., and J.-L. Dufresne, 2005: Marine boundary layer clouds at the heart of tropical cloud feedback uncertainties in climate models. *Geophysical Research Letters*, **32 (20)**.

Bony, S., J.-L. Dufresne, H. Le Treut, J.-J. Morcrette, and C. Senior, 2004: On dynamic and thermodynamic components of cloud changes. *Climate Dynamics*, **22 (2-3)**, 71–86.

Burdanowitz, J., L. Nuijens, B. Stevens, and C. Klepp, 2015: Evaluating light rain from satellite-and ground-based remote sensing data over the subtropical north atlantic. *Journal of Applied Meteorology and Climatology*, **54 (3)**, 556–572.

Chen, R., Z. Li, R. J. Kuligowski, R. Ferraro, and F. Weng, 2011: A study of warm rain detection using a-train satellite data. *Geophysical Research Letters*, **38 (4)**.

Curry, J. A., C. D. Ardeel, and L. Tian, 1990: Liquid water content and precipitation characteristics of stratiform clouds as inferred from satellite microwave measurements. *Journal of Geophysical Research: Atmospheres*, **95 (D10)**, 16 659–16 671.

Dee, D., and Coauthors, 2011: The era-interim reanalysis: Configuration and performance of the data assimilation system. *Quarterly Journal of the royal meteorological society*, **137 (656)**, 553–597.

Duong, H., A. Sorooshian, and G. Feingold, 2011: Investigating potential biases in observed and modeled metrics of aerosol-cloud-precipitation interactions. *Atmospheric Chemistry and Physics*, **11 (9)**, 4027–4037.

Ellis, T. D., T. L'Ecuyer, J. M. Haynes, and G. L. Stephens, 2009: How often does it rain over the global oceans? the perspective from cloudsat. *Geophysical Research Letters*, **36 (3)**.

Fox, N. I., and A. J. Illingworth, 1997: The potential of a spaceborne cloud radar for the detection of stratocumulus clouds. *Journal of Applied Meteorology*, **36 (6)**, 676–687.

Gerber, H., 1996: Microphysics of marine stratocumulus clouds with two drizzle modes. *Journal of the atmospheric sciences*, **53 (12)**, 1649–1662.

Gilbert, G. K., 1884: *Finley's tornado predictions*. Burr.

Guo, H., Y. Liu, and J. Penner, 2008: Does the threshold representation associated with the autoconversion process matter? *Atmospheric Chemistry and Physics*, **8 (5)**, 1225–1230.

Haynes, J. M., T. S. L'Ecuyer, G. L. Stephens, S. D. Miller, C. Mitrescu, N. B. Wood, and S. Tanelli, 2009: Rainfall retrieval over the ocean with spaceborne w-band radar. *Journal of Geophysical Research: Atmospheres*, **114 (D8)**.

Hong, Y., C. D. Kummerow, and W. S. Olson, 1999: Separation of convective and stratiform precipitation using microwave brightness temperature. *Journal of Applied Meteorology*, **38 (8)**, 1195–1213.

Kidd, C., and P. Joe, 2007: Importance, identification and measurement of light precipitation at mid-to high latitudes. *Proc. Joint EUMETSAT Meteorol. Satellite Conf. and the 15th Sat. Meteor. & Ocean. Conf. American Meteorological Society, Amsterdam*.

King, J. M., C. D. Kummerow, S. C. Van Den Heever, and M. R. Igel, 2015: Observed and modeled warm rainfall occurrence and its relationships with cloud macrophysical properties. *Journal of the Atmospheric Sciences*, **72 (11)**, 4075–4090.

King, M. D., S.-C. Tsay, S. E. Platnick, M. Wang, and K.-N. Liou, 1997: Cloud retrieval algorithms for modis: Optical thickness, effective particle radius, and thermodynamic phase. Tech. rep.

Kubar, T. L., D. L. Hartmann, and R. Wood, 2009: Understanding the importance of microphysics and macrophysics for warm rain in marine low clouds. part i: Satellite observations. *Journal of the Atmospheric Sciences*, **66 (10)**, 2953–2972.

Kummerow, C., and R. Ferraro, 2007: Algorithm theoretical basis document: Eos/amsr-e level-2 rainfall. Tech. rep.

Kummerow, C., W. S. Olson, and L. Giglio, 1996: A simplified scheme for obtaining precipitation and vertical hydrometeor profiles from passive microwave sensors. *IEEE Transactions on Geoscience and Remote Sensing*, **34 (5)**, 1213–1232.

Kummerow, C., and Coauthors, 2001: The evolution of the goddard profiling algorithm (gprof) for rainfall estimation from passive microwave sensors. *Journal of Applied Meteorology*, **40 (11)**, 1801–1820.

Kummerow, C. D., S. Ringerud, J. Crook, D. Randel, and W. Berg, 2011: An observationally generated a priori database for microwave rainfall retrievals. *Journal of Atmospheric and Oceanic Technology*, **28 (2)**, 113–130.

Lafont, D., and B. Guillemet, 2004: Subpixel fractional cloud cover and inhomogeneity effects on microwave beam-filling error. *Atmospheric research*, **72 (1)**, 149–168.

Lau, K., and H. Wu, 2003: Warm rain processes over tropical oceans and climate implications. *Geophysical Research Letters*, **30 (24)**.

Lau, K.-M., and H.-T. Wu, 2011: Climatology and changes in tropical oceanic rainfall characteristics inferred from tropical rainfall measuring mission (trmm) data (1998–2009). *Journal of Geophysical Research: Atmospheres*, **116 (D17)**.

Lebsock, M. D., and T. S. L'Ecuyer, 2011: The retrieval of warm rain from cloudsat. *Journal of Geophysical Research: Atmospheres*, **116 (D20)**.

Lebsock, M. D., T. S. L'Ecuyer, and G. L. Stephens, 2011: Detecting the ratio of rain and cloud water in low-latitude shallow marine clouds. *Journal of Applied Meteorology and Climatology*, **50 (2)**, 419–432.

Lebsock, M. D., G. L. Stephens, and C. Kummerow, 2008: Multisensor satellite observations of aerosol effects on warm clouds. *Journal of Geophysical Research: Atmospheres*, **113 (D15)**.

L'Ecuyer, T. S., W. Berg, J. Haynes, M. Lebsock, and T. Takemura, 2009: Global observations of aerosol impacts on precipitation occurrence in warm maritime clouds. *Journal of Geophysical Research: Atmospheres*, **114 (D9)**.

L'Ecuyer, T. S., and J. H. Jiang, 2010: Touring the atmosphere aboard the a-train. *Phys. Today*, **63 (7)**, 36–41.

L'Ecuyer, T. S., and G. L. Stephens, 2002: An estimation-based precipitation retrieval algorithm for attenuating radars. *Journal of applied meteorology*, **41 (3)**, 272–285.

Lensky, I. M., and D. Rosenfeld, 1997: Estimation of precipitation area and rain intensity based on the microphysical properties retrieved from noaa avhrr data. *Journal of Applied Meteorology*, **36 (3)**, 234–242.

Leon, D. C., Z. Wang, and D. Liu, 2008: Climatology of drizzle in marine boundary layer clouds based on 1 year of data from cloudsat and cloud-aerosol lidar and infrared pathfinder satellite observations (calipso). *Journal of Geophysical Research: Atmospheres*, **113 (D8)**.

Liu, C., and E. J. Zipser, 2009: "warm rain" in the tropics: Seasonal and regional distributions based on 9 yr of trmm data. *Journal of Climate*, **22 (3)**, 767–779.

Ma, C.-C., C. R. Mechoso, A. W. Robertson, and A. Arakawa, 1996: Peruvian stratus clouds and the tropical pacific circulation: A coupled ocean-atmosphere gcm study. *Journal of Climate*, **9 (7)**, 1635–1645.

Mace, G. G., and Q. Zhang, 2014: The cloudsat radar-lidar geometrical profile product (rl-geoprof): Updates, improvements, and selected results. *Journal of Geophysical Research: Atmospheres*, **119 (15)**, 9441–9462.

Masunaga, H., T. Y. Nakajima, T. Nakajima, M. Kachi, and K. Suzuki, 2002: Physical properties of maritime low clouds as retrieved by combined use of tropical rainfall measuring mission (trmm) microwave imager and visible/infrared scanner 2. climatology of warm clouds and rain. *Journal of Geophysical Research: Atmospheres*, **107 (D19)**.

Medeiros, B., and B. Stevens, 2011: Revealing differences in gcm representations of low clouds. *Climate dynamics*, **36 (1-2)**, 385–399.

Miller, M., and S. Yuter, 2013: Detection and characterization of heavy drizzle cells within subtropical marine stratocumulus using amsr-e 89-ghz passive microwave measurements. *Atmospheric Measurement Techniques*, **6 (1)**, 1–13.

Mitrescu, C., T. L'Ecuyer, J. Haynes, S. Miller, and J. Turk, 2010: Cloudsat precipitation profiling algorithm-model description. *Journal of Applied Meteorology and Climatology*, **49 (5)**, 991–1003.

Morrissey, M. L., and J. E. Janowiak, 1996: Sampling-induced conditional biases in satellite climate-scale rainfall estimates. *Journal of Applied Meteorology*, **35 (4)**, 541–548.

Nauss, T., and A. Kokhanovsky, 2006: Discriminating raining from non-raining clouds at mid-latitudes using multispectral satellite data. *Atmospheric Chemistry and Physics*, **6 (12)**, 5031–5036.

O'Dell, C. W., F. J. Wentz, and R. Bennartz, 2008: Cloud liquid water path from satellite-based passive microwave observations: A new climatology over the global oceans. *Journal of Climate*, **21 (8)**, 1721–1739.

Petty, G. W., 1995: Frequencies and characteristics of global oceanic precipitation from shipboard present-weather reports. *Bulletin of the American Meteorological Society*, **76 (9)**, 1593–1616.

Petty, G. W., 1999: Prevalence of precipitation from warm-topped clouds over eastern asia and the western pacific. *Journal of climate*, **12 (1)**, 220–229.

Randall, D., J. Coakley, C. Fairall, R. Kropfli, and D. Lenschow, 1984: Outlook for research on marine subtropical stratocumulus clouds. *Bull. Amer. Meteor. Soc*, **65**, 1290–1301.

Rapp, A. D., G. Elsaesser, and C. Kummerow, 2009: A combined multisensor optimal estimation retrieval algorithm for oceanic warm rain clouds. *Journal of Applied Meteorology and Climatology*, **48 (11)**, 2242–2256.

Rapp, A. D., M. Lebsock, and T. L'Ecuyer, 2013: Low cloud precipitation climatology in the southeastern pacific marine stratocumulus region using cloudsat. *Environmental Research Letters*, **8 (1)**, 014 027.

Rosenfeld, D., and G. Gutman, 1994: Retrieving microphysical properties near the tops

of potential rain clouds by multispectral analysis of avhrr data. *Atmospheric research*, **34 (1)**, 259–283.

Schumacher, C., and R. A. Houze, 2003: The trmm precipitation radar's view of shallow, isolated rain. *Journal of Applied Meteorology*, **42 (10)**, 1519–1524.

Sekiguchi, M., T. Nakajima, K. Suzuki, K. Kawamoto, A. Higurashi, D. Rosenfeld, I. Sano, and S. Mukai, 2003: A study of the direct and indirect effects of aerosols using global satellite data sets of aerosol and cloud parameters. *Journal of Geophysical Research: Atmospheres*, **108 (D22)**.

Seto, S., N. Takahashi, and T. Iguchi, 2005: Rain/no-rain classification methods for microwave radiometer observations over land using statistical information for brightness temperatures under no-rain conditions. *Journal of applied meteorology*, **44 (8)**, 1243–1259.

Shao, H., and G. Liu, 2004: Detecting drizzle in marine warm clouds using combined visible, infrared, and microwave satellite data. *Journal of Geophysical Research: Atmospheres (1984–2012)*, **109 (D7)**.

Short, D. A., and K. Nakamura, 2000: Trmm radar observations of shallow precipitation over the tropical oceans. *Journal of Climate*, **13 (23)**, 4107–4124.

Simpson, J., R. F. Adler, and G. R. North, 1988: A proposed tropical rainfall measuring mission (trmm) satellite. *Bulletin of the American meteorological Society*, **69 (3)**, 278–295.

Simpson, J., C. Kummerow, W.-K. Tao, and R. F. Adler, 1996: On the tropical rainfall measuring mission (trmm). *Meteorology and Atmospheric physics*, **60 (1-3)**, 19–36.

Snodgrass, E. R., L. Di Girolamo, and R. M. Rauber, 2009: Precipitation characteristics of trade wind clouds during rico derived from radar, satellite, and aircraft measurements. *Journal of Applied Meteorology and Climatology*, **48 (3)**, 464–483.

Stephens, G. L., and J. M. Haynes, 2007: Near global observations of the warm rain

coalescence process. *Geophysical Research Letters*, **34 (20)**.

Stephens, G. L., and Coauthors, 2002: The cloudsat mission and the a-train: A new dimension of space-based observations of clouds and precipitation. *Bulletin of the American Meteorological Society*, **83 (12)**, 1771–1790.

Stephens, G. L., and Coauthors, 2010: Dreary state of precipitation in global models. *Journal of Geophysical Research: Atmospheres*, **115 (D24)**.

Suzuki, K., and G. L. Stephens, 2009: Relationship between radar reflectivity and the time scale of warm rain formation in a global cloud-resolving model. *Atmospheric Research*, **92 (4)**, 411–419.

Suzuki, K., G. L. Stephens, S. C. Van Den Heever, and T. Y. Nakajima, 2011: Diagnosis of the warm rain process in cloud-resolving models using joint cloudsat and modis observations. *Journal of the Atmospheric Sciences*, **68 (11)**, 2655–2670.

Wang, Y., Y. Chen, Y. Fu, and G. Liu, 2016: Identification of precipitation onset based on cloudsat observations. *Journal of Quantitative Spectroscopy and Radiative Transfer*.

Wentz, F., 1990: Sbir phase ii report: West coast storm forecasting with ssm/i, rss tech. Rpt.

Wentz, F. J., 1997: A well-calibrated ocean algorithm for special sensor microwave/imager. *Journal of Geophysical Research: Oceans*, **102 (C4)**, 8703–8718.

Westwater, E. R., 1972: *Microwave emission from clouds*, Vol. 55. Environmental Research Laboratories.

Wilheit, T., A. Chang, M. V. Rao, E. Rodgers, and J. S. Theon, 1977: A satellite technique for quantitatively mapping rainfall rates over the oceans. *Journal of applied meteorology*, **16 (5)**, 551–560.

Wilheit, T. T., 1986: Some comments on passive microwave measurement of rain. *Bulletin of the American Meteorological Society*, **67 (10)**, 1226–1232.

Wilks, D. S., 2011: *Statistical methods in the atmospheric sciences*, Vol. 100. Academic

press.

Winker, D. M., M. A. Vaughan, A. Omar, Y. Hu, K. A. Powell, Z. Liu, W. H. Hunt, and S. A. Young, 2009: Overview of the calipso mission and caliop data processing algorithms. *Journal of Atmospheric and Oceanic Technology*, **26 (11)**, 2310–2323.